DESIGN AND ANALYSIS OF WAVY FLAT PLATE HEAT PIPE FOR BIDIRECTIONAL THERMAL MANAGEMENT OF LI-ION BATTERY MODULES

Lappeenranta–Lahti University of Technology LUT

Master's Programme in Sustainable Energy Systems, Master's Thesis

2025

Md Mohiuddin Soroj

Examiner(s): Professor Teemu Turunen-Saaresti

Professor Pertti Kauranen

ABSTRACT

Lappeenranta–Lahti University of Technology LUT

LUT School of Energy Systems

Energy Technology

Md Mohiuddin Soroj

Design and Analysis of Wavy Flat Plate Heat Pipe for Bidirectional Thermal Management of Li-ion Battery Modules

Master's thesis

2025

82 pages, 24 figures, and 17 tables

Examiner(s): Professor Teemu Turunen-Saaresti and Professor Pertti Kauranen

Keywords: Hybrid Thermal Management System (HTMS), Heat Pipe Wick Structures, Wavy Flat Plate Heat Pipe (WFPHP), Bidirectional Thermal Management, HVAC Integration

The design and assessment of a wavy flat plate heat pipe based system for the bidirectional thermal control of lithium-ion battery modules utilized in electric vehicles (EVs) are presented in this thesis. Minimizing intra pack temperature gradients and preserving a steady operating temperature between 20°C and 45°C are essential for Li-ion batteries' thermal performance. It is sometimes difficult for traditional systems to attain sufficient thermal uniformity and control in dynamic load and environmental situations.

The suggested wavy flat plate heat pipe and integrated system combine with the refrigeration cycle to provide heating and cooling capabilities. Acetone is chosen because of its advantageous thermophysical characteristics, such as its low viscosity and high latent heat. By using the capillary action of acetone as the working fluid of the designed heat pipe, the design makes it possible to regulate the temperature consistently, independent of orientation. For increased thermal efficiency and compactness, the system can also be directly integrated with a car's HVAC loop.

The findings show that compared to conventional techniques, the WFPHP system greatly enhances temperature uniformity, responsiveness, and bidirectional capability. It promises efficient heat transport, HVAC compatibility, and small size, making it a viable option for long term battery thermal management in next generation EVs.

SYMBOLS AND ABBREVIATIONS

Roman characters

A	Area	m^2
Cp	Heat capacity	J/(g K);
d	Diameter	m
K	Heat conductance	(kW/◦C)
m	Mass	Kg
p	pressure	bar, Pa
q_m	mass flow rate	kg/s
Q	Heat generating power	(W)
q	thermal conductivity	W/m.k
R	Thermal resistance	ºC/W or K/W
T	temperature	ºC, K
t	time	s (second)
U	heat transfer coefficient	$W/(m^2 \cdot K)$
V	volume	m^3
v	specific volume	m^3/kg
X, Y, Z	Coordinates	-

Greek characters

α	Incidence angle	°
λ	Wavelength	m
η	Efficiency	%
ρ_f	Fluid density	kg/m^3
ρ_s	Solid density	kg/m^3

μ_f	Fluid dynamic viscosity	kg/ms
σ	Surface tension of fluid	N/m

Constants

g	gravitational acceleration	9,81 m/s

Abbreviations

AC	Alternating Current
BMS	Battery Management System
BTMS	Battery Thermal Management System
CAD	Computer Aided Design
CFD	Computational Fluid Dynamics
COP	Coefficient of Performance
EC_NRV	Electrically Controlled Non Return Valve
ECV	Electrically Controlled Valve
EEV	Electronic Expansion Valve
EV	Electric Vehicle
GWP	Global Warming Potential
HEV	Hybrid Electric Vehicle
HFC	Hydrofluorocabons
HFO	Hydrofluoro-olefins
HP	Heat Pipe
HTMS	Hybrid Thermal Management System

HVAC	Heating, Ventilation, and Air Conditioning
ICE	Internal Combustion Engine
LCA	Life Cycle Assessment
LEL	Lower Explosive Limit
LHP	Loop Heat Pipe
LIB	Lithium-Ion Battery
MFPHP	Micro Flat Plate Heat Pipe
NCA	Nickel Cobalt Aluminium
NMC	Nickel Manganese Cobalt
Nu	Nusselt number
ODP	Ozone Depletion Potential
PCM	Phase change material
PEC	Performance evaluation criteria
PHP	Pulsating Heat Pipe
Pr	Prandtl number
PTC	Positive Temperature Coefficient Heater
SEI	Solid Electrolyte Interphase
SHLB	Self Heating Lithium ion Battery
SOC	State of Charge
TMS	Thermal Management System
TRL	Technology Readiness Level
VC	Vapor Chamber
VCC	Vapor Compression Cycle
WFPHP	Wavy Flat Plate Heat Pipe

WLTC	Worldwide Harmonized Light Vehicles Test Cycle

Subscripts

amb	Ambient
avg	Average
b	Volume
batt	Battery
bid	Bidirectional Heat Exchanger
cab	Cabin
ch	Channel
con	Condenser
cond	Conduction
conv	Convection
eva	Evaporator
ext	External
f	Fluid
g	Gravity
in	Inlet
j	Joule heat
l	Liquid
max	Maximum
n	number of channels
n1	number of channels on one side
n2	number of channels on the other side

new	updated
p	Polarization
r	Reaction
s	Solid
tot	Total
v	Vapor
int	Internal
W	Wall
w	wetted area

Table of contents

Abstract

(Acknowledgements)

(Symbols and abbreviations)

Declarations

Contents

ACKNOWLEDGEMENTS

First and foremost, I want to profoundly appreciate my supervisors, Prof. Teemu Turunen-Saaresti and Prof. Pertti Kauranen, for their unwavering support, knowledgeable direction, and insightful criticism during the composition of this thesis. Their advice, support, and tolerance have been invaluable in guiding me through the academic and technical facets of this study.

Personally, I want to express my gratitude to my family for their unwavering support, love, and encouragement. Throughout my academic career, their confidence in me has been a continual source of support.

Lastly, I would like to express my gratitude to everyone who helped make this thesis possible, whether directly or indirectly. Each and every suggestion, criticism, and support has had a significant influence on this work.

With sincere appreciation,

Md Mohiuddin Soroj

Figures

Tables

DECLARATIONS

Turnitin

The originality of this thesis has been reviewed with the Turnitin similarity checking service.

AI usage

The author of this thesis, Md Mohiuddin Soroj, did not use any AI tools during the preparation of the thesis**.**

Responsibility

The author, Md Mohiuddin Soroj, takes full responsibility for the content of this thesis and has reviewed and edited the content generated by the possible use of AI tools.

1 Introduction

Electric vehicles (EVs) are considered potential substitutes for conventional fuel powered vehicles because they offer the best opportunities for the utilization of new energy sources in transportation and zero carbon emissions. In comparison to traditional secondary batteries, rechargeable lithium-ion (Li-ion) batteries exhibit superior energy density, enhanced power output, and extended cycle life, rendering them optimal and extensively utilized as power sources for electric vehicles (EVs). The battery's temperature rises due to the heat generated by the internal chemical reaction and the ohmic internal resistance during the charging and discharging cycles.(Guo & Jiang 2021). Also, uncontrolled battery temperature drops can also lower a number of important parameters, including lithium diffusion and electrolyte conductivity, since they increase electric and electrochemical losses. This poses significant challenges for nations such as China, Europe, and the United States, where winter temperatures fall below 0 °C. These challenges are worse after -20 °C (Maiorino et al. 2024). According to (Wang et al. 2016; Liu et al. 2017) The ideal operating temperature range for Li-ion batteries, in terms of longevity and safety, is between 20 °C and 45 °C. So, depending on the environment and driving circumstances, the batteries' needs for heating and cooling should be taken into consideration. Additionally, to maintain the battery's intended state of health and improve performance, the temperature throughout the battery pack should be kept as consistent as feasible. Consequently, an advanced battery thermal management system that can precisely regulate temperature in a variety of year round climates is ideal for electric vehicles (Guo et al. 2021). Unexpected internal heat exchanges may result from excessive fluctuation between cells. According to He et al. 2023 , it is essential to uphold a uniform temperature distribution throughout the battery pack, and the internal temperature variation must not surpass 5 °C. This demonstrates that a comprehensive, vehicle wide thermal management system is now necessary rather than optional. So, an effective battery thermal management system (BTMS) must be designed not only to dissipate surplus energy effectively, but also actively regulate battery temperatures, preserve passenger comfort, and adjust to wildly fluctuating outside weather conditions in a sustainable way.

Numerous BTMS strategies have been researched previously in order to address these issues. Particularly promising are two phase heat transfer devices, like heat pipes, which offer

extremely high effective thermal conductivity (sometimes known as "superconductors" of heat) with little temperature loss (Boonma et al. 2022). Specifically, thin, flat heat pipes may be made flexible and lightweight, and they have a lot of surface area that comes in contact with the cells, which helps to ensure that the battery module has a consistent temperature (Y. Wang et al. 2022). These benefits serve as the impetus for this thesis, where investigation and design of a bidirectional battery thermal management system that integrates the vehicle's HVAC (Heating, ventilation, and air conditioning) loop with a flexible wavy thin flat plate heat pipe charged with acetone to provide heating and cooling of the battery pack as required.

Several studies have shown a wide variety of BTMS techniques. Indirect liquid cooling, usually using water and glycol, achieves significantly better heat transfer coefficients than conventional air cooling, which is straightforward and inexpensive (Garud et al. 2023). Phase change material (PCM) layers and other hybrid or auxiliary techniques have demonstrated notable advantages in lowering peak temperatures. For example, under high load, some PCMs can reduce cell temperatures by about 30 to 33 °C (A. Afzal et al. 2023); however, their intrinsically low thermal conductivity frequently calls for a combination with other cooling techniques. Results from heat pipe assisted cooling have been further enhanced by numerous experiments that add liquid cooled condensers or aluminum fins to flat or loop heat pipes to improve heat rejection (Boonma et al. 2022). Additionally, according to experimental analysis by Y. Wang et al. (2022), adding flat plate heat pipes between battery cells successfully maintained maximum cell temperatures far below safety limits, staying below 35 °C throughout a 4C (C rating) discharge, and decreased temperature variance to a few degrees. Further demonstrated that a refrigerant cooled flat plate heat pipe can maintain safe cell temperatures in a variety of load and ambient situations.

There are still several gaps despite these advancements. Particularly, in active control and bidirectional heat transfer (to enable both cooling and heating) have mainly gone ignored in the majority of published BTMS designs, which are primarily passive or one way cooling systems. In other words, no previous study has shown a heat pipe array with fluid circuits or flow direction that can be changed or swapped in response to the need for cooling and heating the cells or for other active real time control. Numerous specialists have demonstrated that orientation can significantly affect heat pipe performance (thermal resistance, temperature uniformity). In summary, an actively regulated flat plate heat pipe (FPHP) based BTMS can be a sustainable electric vehicle thermal management system that ensures efficient

bidirectional heat transfer, maintains battery safety and performance, and adapts to varying ambient and operational conditions throughout the year. This BTMS must be able to interface with the existing HVAC loop and be able to both cool and heat the battery in accordance with ambient conditions and stability requirements, all while maintaining performance regardless of gravity orientation. In light of the aforementioned factors, this thesis also aims to answer the following important questions: How can a sustainable BTMS be made to regulate heat in both directions under a variety of climatic conditions? How can sizing and performance be merged together? How can real time temperature control be achieved by integration with HVAC loops? What factors affect the performance of MFPHP along with the integrated system?

2 Battery thermal management system design concepts and frameworks

Electric Vehicles (EVs) are pivotal in the current industrial sustainability movement and are recognized as a viable means to mitigate greenhouse gas emissions while tackling global warming. Battery thermal management is an essential component of EV development that guarantees high performance, competitiveness in the market, and environmental sustainability. High or low operating temperatures are known to have negative impacts on battery life and performance. From the perspective of the operator or customer, the cars would be better overall in terms of all electric range and performance, comfort, and safety if the current Battery Thermal Management Systems (BTMS) technologies were improved (Guo & Jiang 2021). According to M. Bernagozzi et al. 2023, there are currently just two BTMS technologies used in commercial vehicles: liquid cooling and air cooling. To follow the purpose of the thesis, existing studies regarding potential technologies applicable to the Heat Pipe based BTMS system will be analyzed. This analysis aims to compile the findings from various studies, pointing out both advantages and disadvantages of each sector, starting with analyzing existing BTMS strategies, choosing a suitable strategy, modifying and analyzing the strategy for the Heat pipe (HP) integration will be one of the fundamental steps to reach the goal of this thesis.

2.1 Existing battery thermal management system strategies.

A number of studies have been reported in the field of Thermal management systems (TMS) and several TMSs have been developed in recent years. The following technologies have been confirmed to have been developed over the years and key findings by (Maiorino et al. 2024) have been reported in Table 1.

Table 1: Comparison of the different TMSs used for the EV battery packs. (Maiorino et al. 2024)

TMS	Type	Advantages	Disadvantages
Air	External heating/cooling	• High reliability • Low cost •Simply maintenance	• Low efficiency • Dust and pollutants in the ducts
Liquid	External heating/cooling	• High efficiency of the heat exchange • Low energy demand	• High number of components • High cost of installation and maintenance
Refrigerant	External heating/cooling	• Best efficiency of the heat exchange • Low impact on the weight of the vehicle	• High complexity of the plant • Not all refrigerant based systems support reversible operation for both heating and cooling modes.
PCM	External heating/cooling	• Fixed temperature during the phase change • Do not require additional electric power	• Low thermal conductivity, which does not allow heat dissipation during cooling down • The addition of conductive materials may produce fires
Heat Pipes	External heating/cooling	• Do not require any additional electric power • Low maintenance • High thermal conductivity	• Small contact area • Thermal management is not always reached • No stand alone applications
Internal Strategies	Internal heating only	• High heating efficiency • High heating rates • Good temperature uniformity	• AC preheating needs an external energy source • High degradation of the battery pack due to the formation of Li-ion plating

Heat pipes, PCM and internal strategies are passive TMSs since they don't require any electric energy source; on the other hand, the first three (Air, liquid and refrigerant) are active TMSs since they need power to function. A Hybrid Thermal Management System (HTMS), which consists of at least two of these systems, is created when they are combined.

The battery pack is immediately warmed by the heat produced by the polarization losses that occur when current enters the cells. By raising the battery pack's internal temperature, the

second cluster of procedures can swiftly create a uniform temperature field and lessen thermal energy dispersions into the surrounding environment. Four main internal heating strategies are reported by (Maiorino et al. 2024)

- Internal self heating.
- Mutual pulse heating.
- Self Heating Lithium ion Battery (SHLB).
- Alternating current heating

Internal self heating is a battery warm up technique where the battery's internal resistances, such as polarization and ohmic resistance, are the only source of heat generation in internal self heating techniques. Because lithium plating is likely to occur when batteries are charged at low temperatures, they must use some of their stored energy to heat themselves internally through discharging. The battery and another energy reservoir (such as batteries or capacitors) are used in mutual pulse heating to create an electric circuit and carry out the charge/discharge operation. Two energy reservoirs can be warmed from below freezing temperatures by the bidirectional current pulses produced during this operation. In Self Heating Lithium-ion Battery (SHLB), Internal heat generation is produced using specialized nickel foil that is integrated into batteries. Localized rapid ohmic heating is produced by rerouting battery energy through the foil to energize it selectively. where a switch to connect or disconnect the foil and an integrated activation terminal (ACT) are also included. Unlike Internal self heating, there is no need for external load or cycling because heating is internal and self sufficient. In order to produce heat inside the cell, Alternating Current (AC) heating usually uses an AC as the input signal at the battery terminals. The battery is able to maintain a rather steady state of charge thanks to the quick and regular charging and draining procedures. In contrast to the three internal preheating categories listed above, this kind of approach may typically be accomplished using an external power source during warm up without requiring additional battery energy. Furthermore, when compared to external warm up techniques, AC heating was shown to be one of the most effective preheating methods, heating the battery rapidly and consistently. (Hu et al. 2020)

2.2 Refrigerant based thermal management system

Refrigerant based TMS is considered a subcategory of liquid BTMS, whereas another option is a coolant based system (e.g., water, glycol, oil, or acetone). In a refrigerant based system, the battery heat is absorbed as the refrigerant goes through a phase change process after flowing straight into the battery pack's cooling plate. (Shahjalal et al. 2021). Refrigerant based TMS basically runs on vapor compression refrigeration cycle (VCC), illustrated on Figure 1. Using two evaporators, which lowers the battery pack's average temperature, batteries can be cooled using compression vapor cycles, parallel with EV's HVAC system. The heat exchange efficiency is the primary benefit that these systems provide. As opposed to liquids and gases, two phase heat exchange is known to achieve the largest convective heat transfer coefficient, and its processing temperature stays constant. Additionally, the constant temperature makes it possible to regulate ideal conditions for Li-ion battery thermal management and achieve a more consistent temperature field (Shahjalal et al. 2021). The integration of EV's HVAC systems with refrigerant based battery thermal management systems (BTMS) for cooling purpose has been examined in several research studies before. (Li et al. 2023)

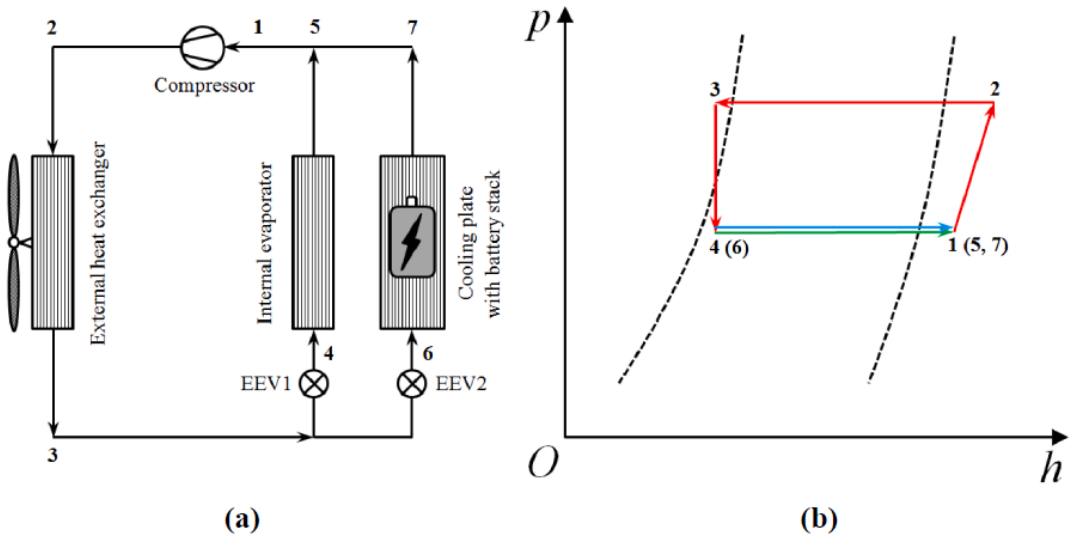

Figure 1: (a) Schematic of basic refrigerant based TMS; (b) Corresponding *p-h* diagram. (Guo & Jiang 2021)

Despite the cooling strategy of VCC, it can also be used for heating purposes too similarly to the working principle of the heat pump. Heat pump operates on the inverse cycle of the VCC. In Figure 2, by (Guo & Jiang 2021), the developed vehicle integrated TMS linking the BTMS and the AC/HP system is depicted. The system consists of a compressor, battery cooling plate, exterior heat exchanger, accumulator, internal cabin evaporator and condenser, three way valves, flow regulation valves, electronic expansion valves (EEV), and check valves. EEVs, flow regulation valves, and three way valves can all be controlled to change the operating mode for various operating situations. In order to regulate the cabin's temperature, installed HVAC system with the interior ventilation channel in the internal evaporator and internal condenser unit has not been illustrated in Figure 2. The cooling plate might be provided with either low temperature or high temperature flowing refrigerant, depending on whether the battery needs to be heated or cooled. The previously stated postpositional throttle valve of the battery cooling plate, the electronic expansion valve EEV3, is used to adjust the refrigerant evaporating temperatures in the internal evaporator and the cooling plate.

Figure 3(a) shows the flow circuit for the cabin and battery combined cooling mode. The compressor compresses the gaseous phase of the refrigerant prior to its entry into the external heat exchanger, which operates as an external condenser. After passed out of the external condenser unit, the refrigerant divides into two portions. One enters the internal evaporator to cool the cabin after expanding through EEV1. The other portion expanded by EEV2, penetrates the battery pack's cooling plate to cool the battery pack, and then undergoes more depressurization by EEV3. To complete the cycle, the two flows combine before entering the compressor through the accumulator. Figure 1(a) illustrates this flow circuit in an equivalently simplified form.

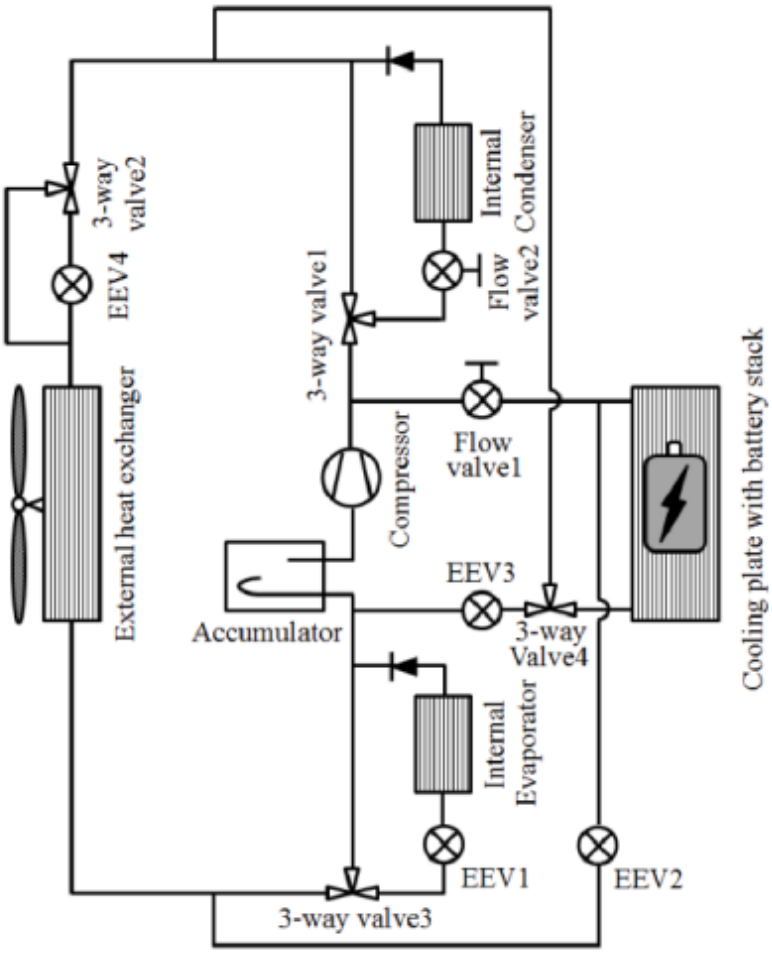

Figure 2: Illustration of the inventive vehicle integrated TMS (Guo & Jiang 2021)

Figure 3(b) shows the flow circuit for the cabin and battery combined heating mode. The flow valves 1 and 2 split the compressor's gaseous refrigerant into two portions, which subsequently enter the cooling plate of the battery and the internal condenser, respectively. After expanding through EEV4, the combined liquid refrigerant from the cooling plate and internal condenser reaches the external heat exchanger, which also functions as an external evaporator.(Guo & Jiang 2021)

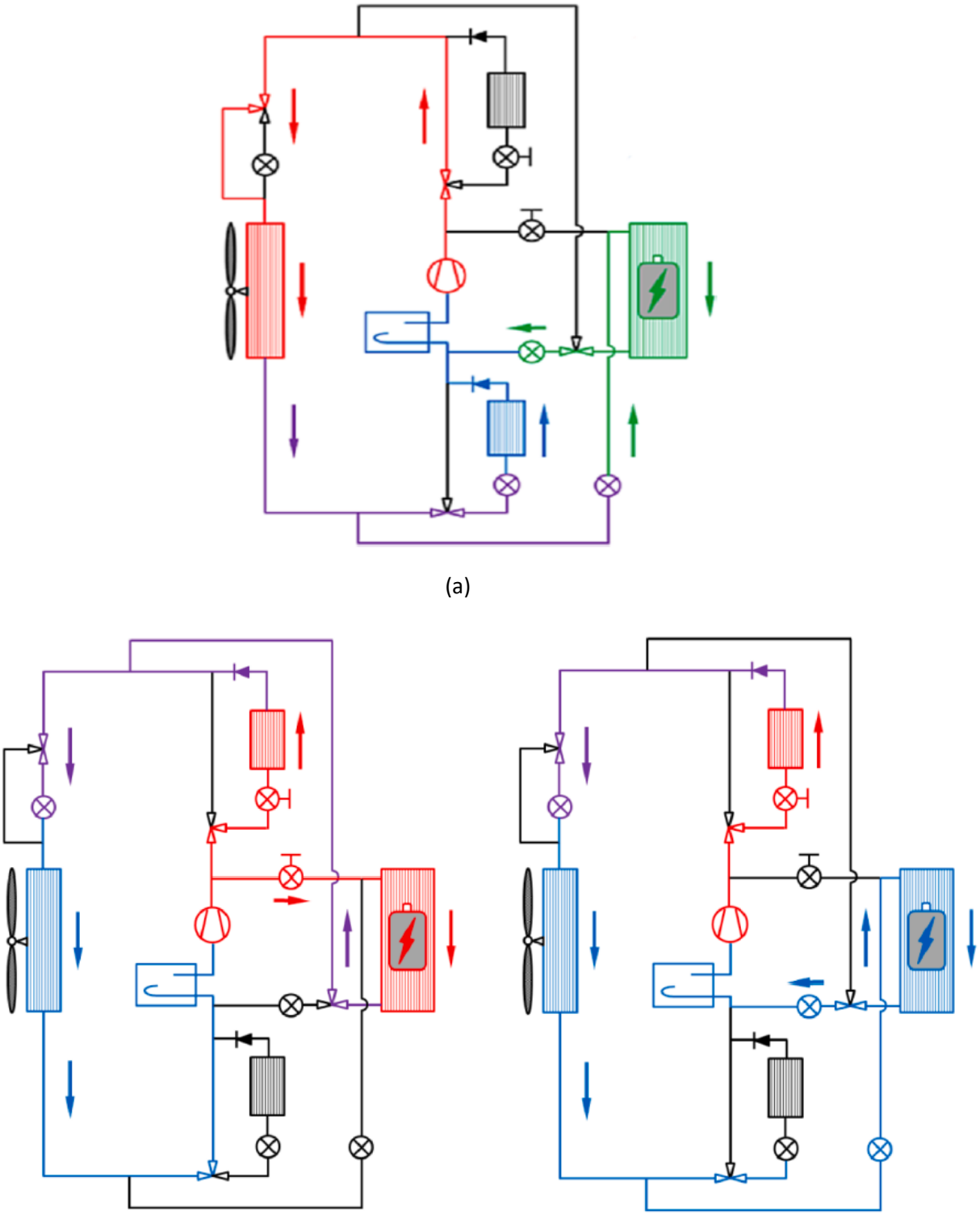

Figure 3: (a) Schematic of the cabin and battery mix cooling mode; (b) schematic of the cabin and battery mix heating mode; (c) schematic of the cabin heating and battery cooling mode. (Guo & Jiang 2021)

In order to complete the refrigeration cycle, the accumulated refrigerant of the external evaporator is then pulled into the compressor. This mode is typically used in the winter to preheat the Li-ion batteries before they reach a temperature high enough to run the vehicle. During this Li-ion battery preheating stage, the compressor can be powered by the same external or backup sources that were used to power the preheating devices of the conventional BTMS (Guo & Jiang 2021).

Figure 3(c) illustrates the flow circuit for the battery cooling and cabin heating modes. After passing through the internal condenser, the compressor's gaseous phase of the refrigerant expands through EEV4 and enters the external heat exchanger, which acts as an external evaporator. In order to complete the cycle, the batteries heat the evaporated refrigerant in the cooling plate even further before it passes through the accumulator and into the compressor. It's crucial to consider that EEV3 and EEV2 should be fully open in this mode to reduce flow resistances and throttling effects. Typically, this mode maintains a warm cabin throughout the winter while utilizing the waste heat extracted from the batteries. (Guo & Jiang 2021)

3 Heat Pipe Analysis

Heat pipes are currently attracting more interest in the field of thermal management of electric vehicle (EV) and hybrid electric vehicle (HEV) battery packs for their superconductive properties, durability, low maintenance requirements, and endurance. Currently, heat pipes are drawing more attention in the thermal management of electric vehicle (EV) and hybrid electric vehicle (HEV) battery packs (D.M. Weragoda et al. 2023).

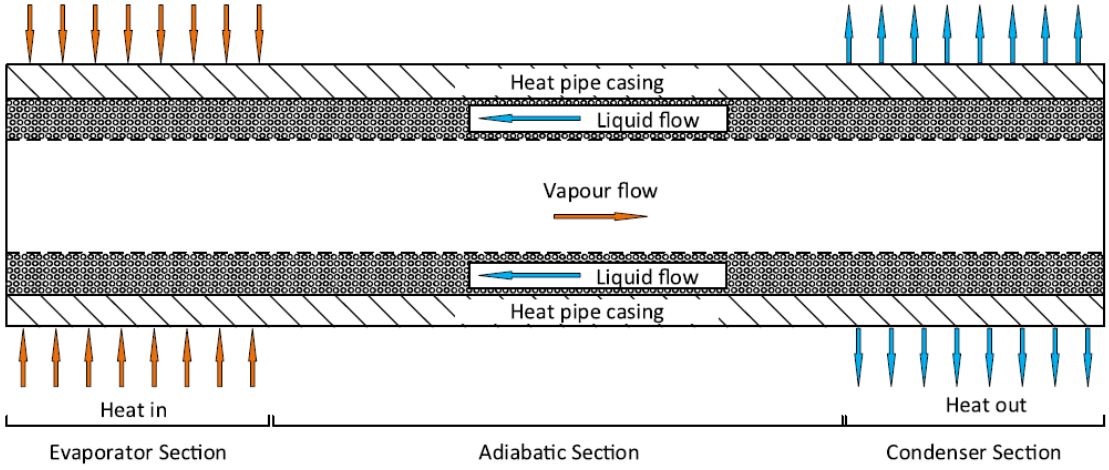

Figure 4: Working schematic of a conventional heat pipe (D.M. Weragoda et al. 2023).

The ability of heat pipes to transfer heat even at extremely low temperature gradients is their most notable characteristic. Through conductive heat transfer, this phenomenon can be used to extract heat produced inside lithium-ion cells from the cell's surface. Heat pipes are devices that use a working fluid to move heat from one location to another. It is a vacuum sealed pipe with working fluid and a wick construction. As seen in Figure 4, the heat pipe is separated into three sections: the condenser, adiabatic, and evaporator. A heat pipe may have more than one evaporator and condenser portion, with or without an adiabatic part, depending on its design and intended use. The heat pipe wall will transmit heat from the heat source to the working fluid. The working fluid transforms from a liquid to a vapor as a result of the heat it absorbs. Phase change can happen at very low temperatures, depending on the working fluid's saturation temperature and pressure as well as the vacuum pressure inside the heat pipe. A heat pipe can carry large heat loads at small temperature gradients thanks to this phase change caused by the latent heat of vaporization. The working fluid is driven from

the evaporator end to the condenser end by the buildup of vapor pressure at the evaporator section. There, it discharges the heat to a sink and condenses the vapor back into liquid. Capillary action pushes this condensate back to the evaporator end through the wick structure, where the cycle is repeated. According to (D.M. Weragoda et al. 2023) , a heat pipe's ability to function continuously is dependent on the capillary pressure it develops. Because of the fluid's surface tension and the size of the pores, the liquid's curved surfaces (menisci) form inside the wick pores. The capillary pressure produced by these menisci helps in returning the liquid to the evaporator and maintains the heat pipe cycle.

3.1 Construction and classification

Heat pipes can be broadly classified into two types: fixed conductance and variable conductance. In contrast to fixed conductance heat pipes, which do not run at a constant temperature, variable conductance heat pipes are able to maintain an operating temperature that is almost constant. A non condensable gas regulates the operating temperature in a variable conductance heat pipe. Heat pipe operating temperatures can be broadly categorized as follows: low temperature (200 K to 500 K), medium temperature (500 K to 750 K), high temperature (750 K and beyond), and cryogenic (0 K to 200 K). These four temperature categories and merit numbers are used to choose the working fluid for heat pipes. (D.M. Weragoda et al. 2023).

Various capillary geometries and wick architecture are used in heat pipes, depending on their application, design, and working fluid. Wick structures that are frequently used include grooved, mesh, and sintered wicks. The wick structure's primary function is to produce the

Additionally, heat pipes are created and produced in various geometrical shapes based on their needs and uses. Capillary driven tubular heat pipes, flat heat pipes, annular heat pipes, loop type heat pipes, pulsating heat pipes, and mini/micro heat pipes are a few of the most popular varieties of heat pipes.

3.2 Heat pipe based battery thermal management

According to (M. Bernagozzi et al. 2023), Heat pipes used for TMS come in three primary varieties: loop heat pipes (LHPs), pulsating heat pipes (PHPs), and traditional or sintered heat pipes (HPs). Figure 5 illustrates the basic structure and the working principle of each of

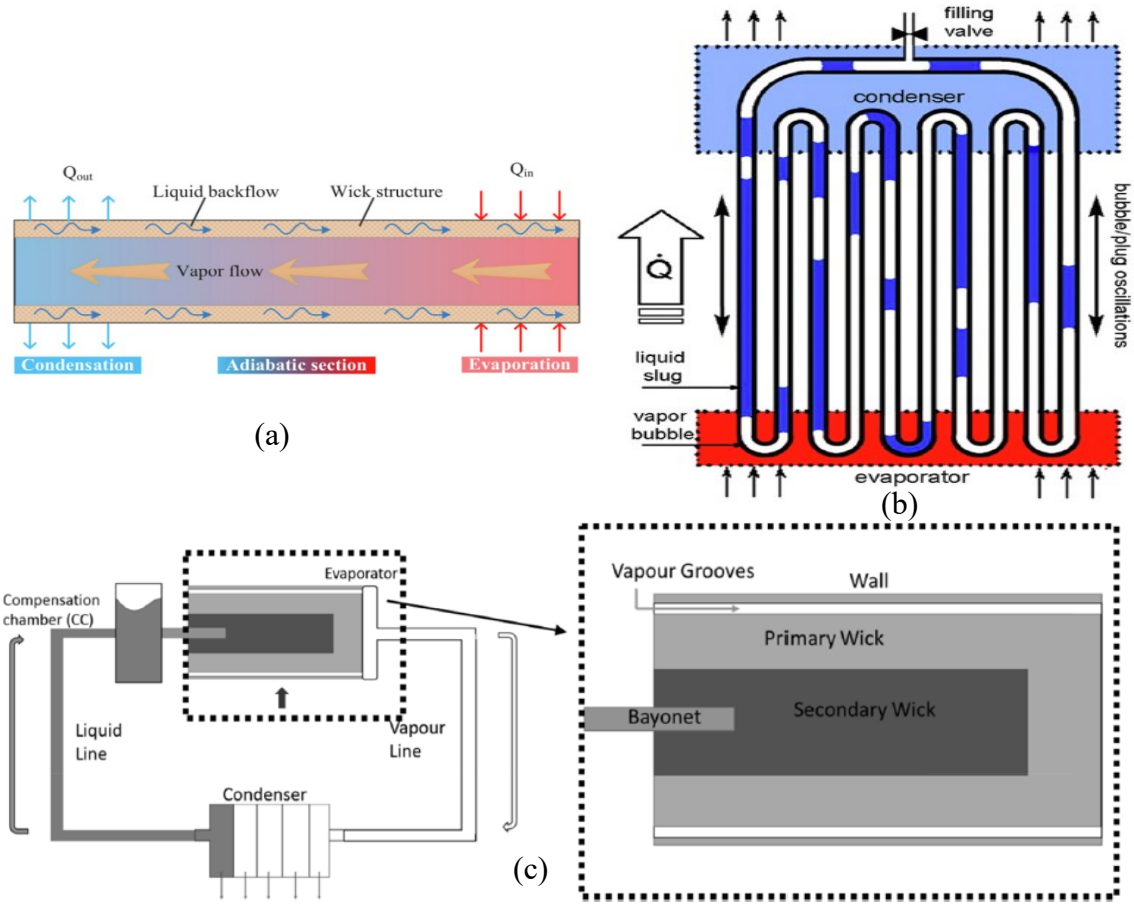

Figure 5: Diagram of the structure and working principle of (a) sintered heat pipes (HPs); (b) pulsating heat pipes (PHPs); (c) loop heat pipes (LHPs). (M. Bernagozzi et al. 2023)

the primary varieties.

Commonly used sintered heat pipes (HP) are evacuated devices that are enclosed by a porous wick that extends the entire length of the device. The working fluid transforms into vapor when heat is provided to the evaporator, one end of the HP. Heat is rejected and condensation happens because of this flowing to the opposite side, known as the condenser, which is in touch with a cold source. Because of the capillarity provided by the wick's tiny pore size, the freshly created liquid returns to the evaporator through the wicked walls.

The Pulsating Heat Pipe (PHP) is a partially functioning fluid filled evacuated meandering tube with an inner diameter below the critical threshold, which permits surface tension to predominate over gravity. As a result, the fluid settles into a series of elements known as liquid slugs and vapor plugs. The evaporation of the liquid coating covering the vapor plugs causes them to expand when heat is delivered to the evaporator, which forces liquid slugs toward the condenser. Here, heat is rejected and the vapor bubble contracts when it comes into contact with the cold source, giving the gadget its distinctive spring like pulsing action that transfers heat. Similar to the passive technologies previously covered, they require a means of heat removal at the condenser; hence, they are not autonomous. Although PHPs for various applications are now commercially available, they cannot be regarded as a unified and dispersed technology since it is challenging to create a PHP with a wide range of applications. According to M. Bernagozzi et al. 2023, the pulsating heat pipes (PHP) has TRLs (Technology Readiness Level) is ranging from 6 to 9. Whereas sintered heat pipes (HP) is 9.

Since the wick is the most expensive component, the Loop Heat Pipe (LHP) is distinguished by having the wicked structure in the evaporator alone, enabling heat transfer over greater distances at a lower price than the same dimension HP. The five primary parts of LHP are as follows: the evaporator, which houses the wick and creates the pressure gradient required for the working fluid to evaporate and flow through the entire apparatus; the liquid and vapor lines, which move the working fluid between its two states; the compensation chamber, which serves the dual purposes of supplying the evaporator with working fluid in the event of a dry out and balancing the pressure variations during operations; and the condenser, which can have a variety of forms and designs as long as it releases the heat that the evaporator absorbs. The LHP functions as a thermal diode and can operate in any gravity orientation because of its evaporator structure.

In recent years, there has been a surge in research on this subject, with numerous technical solutions being examined. A chart illustrating the range of alternatives under study is shown in Figure 6 by (M. Bernagozzi et al. 2023).

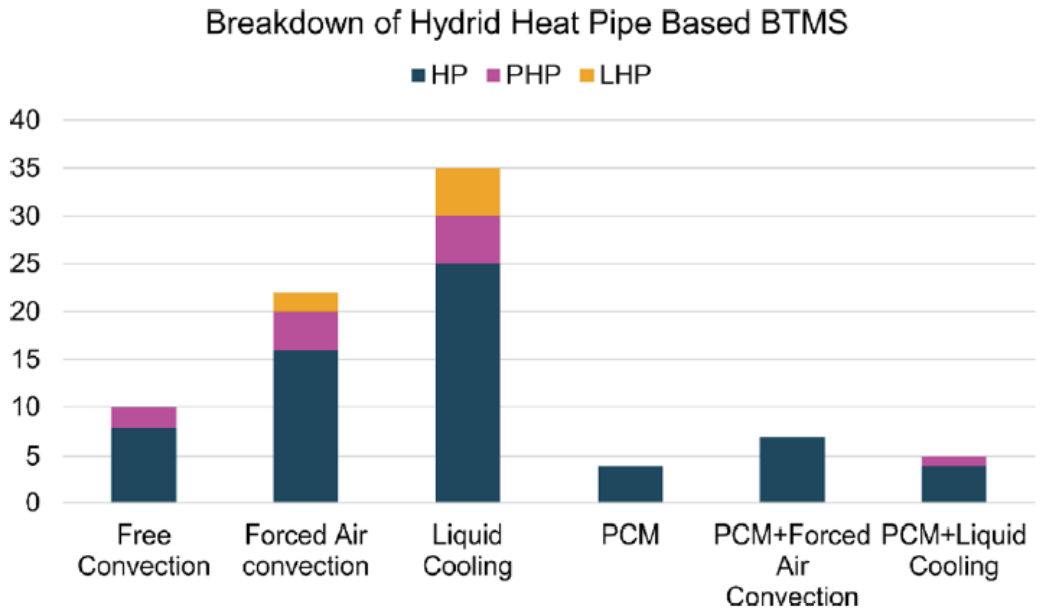

Figure 6: Number of studies based on the coupled complete cooling solution with the hybrid heat pipes for BTMS. (M. Bernagozzi et al. 2023)

Phase Change Material (PCM) integrated heat pipes provide a hybrid thermal management solution by combining heat pipes' strong thermal conductivity with PCMs' latent heat storage capability. This design is particularly useful for lowering peak battery temperatures and smoothing out thermal spikes during quick charge/discharge cycles. According to (M. Bernagozzi et al. 2023), Such hybrid systems improve temperature uniformity and delay critical overheating, making them ideal for high performance EV applications. However, due to their essentially low thermal conductivity, PCMs must be coupled with high efficiency heat pipes to improve transient thermal response.

As per (M. Bernagozzi et al. 2023), most investigations have been done so far on sintered heat pipes (HP). However, PHPs and LHPs in particular are far less popular, probably as a result of their lower TRL in comparison to normal HPs.

M. Bernagozzi et al. 2023, have also shown two alternate heat pipes: 1. Flat Plate Heat pipe (FPHP); 2. Micro Heat Pipe Array (MHPA). Despite the fact that both are designed to meet the flat shape and space requirements of contemporary electronic and battery thermal management applications, their construction, functionality, and thermal performance vary significantly. Flat Plate Heat Pipes (FPHPs) are heat pipes that have flat surfaces for the condenser and evaporator. This makes them perfect for integration into thin or planar parts

such as small electronics and battery modules. FPHPs can also be considered as sintered heat pipes when using sintered wick. In traditional FPHPs, Standard cylindrical heat pipes are mechanically flattened to fit into flat areas (Figure 8, with different degrees of flattening). Due to wick structural deformation and higher hydraulic losses within the flattened vapor core, this approach is economical and permits the use of commercially available components; however, performance is frequently impaired. When the entire pipe is flattened, this deformation improves heat resistance and decreases capillary action (M. Bernagozzi et al. 2023). The vapor chamber, a specially designed flat heat pipe with wick structures on both the top and bottom interior surfaces and more advanced kind. Figure 7 from (Shaeri et al., 2018), illustrates the basic working schematic of the vapor chamber. It is held up by internal columns to keep its shape and make liquid return easier. Excellent heat spreading properties make vapor chambers popular in high power applications like CPUs and EV battery cooling systems (M. Bernagozzi et al. 2023).

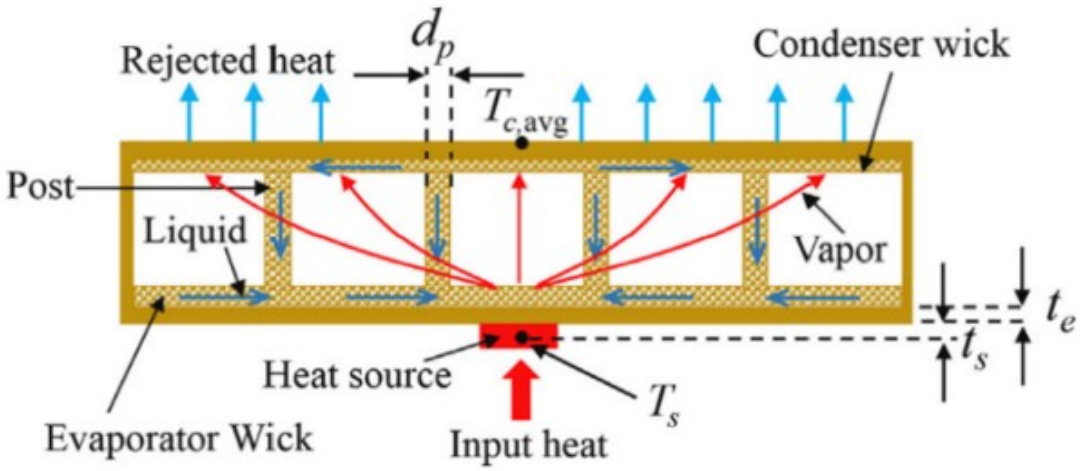

Figure 7: Basic operational schematic of the vapor chamber. (Shaeri et al. 2018)

Micro Heat Pipe Arrays (MHPAs), on the other hand, are made up of several separate micro scale flat heat pipes arranged side by side inside a common substrate. With its own processes for evaporation, condensation, and fluid return, each microchannel operates as an entire heat pipe. Because the entire system is not jeopardized in the event of a single channel failure, this design offers exceptional thermal reliability. A high surface area to volume ratio provided by MHPAs also improves thermal interaction with a variety of surfaces (M. Bernagozzi et al. 2023). Individual channels, however, usually have lower thermal conductivities than a big, cohesive vapor region, such as a vapor chamber. This is brought

on by a smaller working fluid volume, a smaller vapor flow area, and higher capillary resistance per channel.

Considering the flexibilities offered by MHPAs with multiple channel operation, variable range of thermal resistance, individual channel's independent operation and compatibility with variable surfaces can be a suitable choice to fulfill the thesis purpose.

3.3 Performance of flattened heat pipes

To accommodate the space constraint, heat pipes are bent and either fully or partially flattened. The overall thermal resistance (R_o) and the maximum heat load (Q_{max}) determine the performance of heat pipes. The powder wick and the groove wick are two types of wicks that are frequently used in heat pipes applications. Q_{max} may be lowered by a disrupted liquid channel brought on by the collapse of sintered powders. The impedance of heat conduction may rise if the mesh wick or sintered powder peels. Furthermore, the vapor flow may experience hydraulic loss due to the narrowed duct, which would raise R_o. A study carried out by (Lin & Wong 2013) measured important thermal properties such as maximum heat load (Q_{max}), evaporator resistance (R_e), condenser resistance (R_c), and overall thermal resistance (R_o) over different flattening levels using copper/water heat pipes with a 6 mm diameter and 30 cm length. Either the entire length of the heat pipe or the evaporator section underwent flattening, with thicknesses gradually decreased to 3 mm, 2.5 mm, and 2 mm (Figure 8).

According to Lin and Wong's (2013) experimental study, the degree and position of flattening have a major impact on the thermal performance of heat pipes, especially when it involves the type of internal wick structure. Their research showed that limiting the flattening to the evaporator portion did not significantly lower the maximum heat transport capacity (Q_{max}), but rather only slightly increased thermal resistance (R_e). However, there was a noticeable drop in thermal performance when the heat pipe was flattened completely. The mechanisms causing this degradation differed according to the type of wick. It was determined that the most common failure mode for heat pipes with sintered powder wicks was water blockage or clogging at the condenser end. Excess working fluid accumulated inside the porous wick as a result of the fluid channels' high geometric restriction in thin, flattened forms. Due to their high porosity, sintered wicks naturally hold more liquid, which

was exacerbated in the flattened condenser area and prevented liquid from returning to the evaporator. The resulting accumulation of fluid raised condenser thermal resistance and disturbed the heat pipe's phase change cycle. Even with low heat loads, the blockage made the device unable to operate in severe situations, such as heat pipes that had flattened to a thickness of 2.5 mm. Conversely, heat pipes with grooves, which have a lower liquid charge, were less likely to clog. Interfacial shear stresses between the liquid film in the grooves and the vapor flow were the main cause of their performance decline. Despite the fact that overall resistance to condenser blockage was better, these stresses hastened liquid depletion at the evaporator, resulting in early dryout and large reductions in Q_{max}.

The experimental analysis by (Lin & Wong 2013) also found that even in substantially flattened layouts, vapor pressure losses are negligible. As powder wick can hold the liquid in its pores more securely, powdered heat pipes are better protected against interfacial shear, but under the same circumstances, grooved heat pipes are more likely to experience liquid displacement and dry out. However, because to their higher saturated liquid charge, powdered pipes are more prone to condenser blockage. These results, which emphasize the trade offs associated with flattening and provide information on how various wick designs react to geometric limitations, are crucial for manufacturers creating heat pipe based thermal modules.

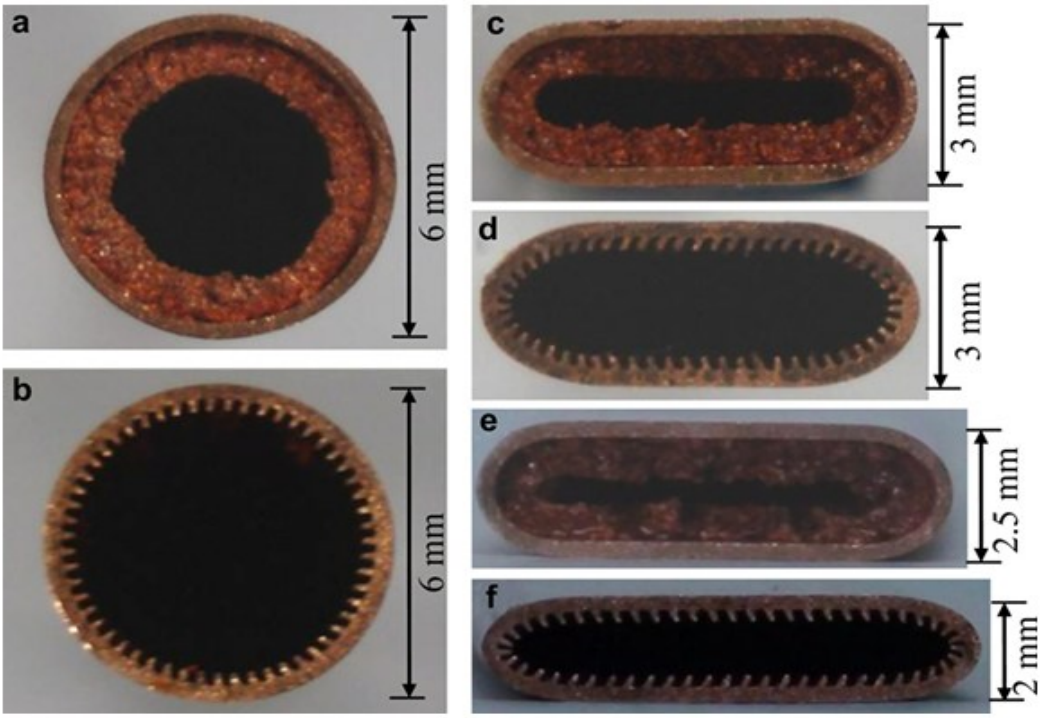

Figure 8: (a) cylindrical heat pipe with a sintered powder wick,; (b) cylindrical heat pipe with a grooved wick structure; (c) 3 mm thick flattened heat pipe with a sintered powder wick; (d) 3 mm thick flattened heat pipe with a grooved wick; (e) 2.5 mm thick flattened heat pipe with a sintered powder wick, and (f) 2 mm thick flattened heat pipe with a grooved wick structure. (Lin & Wong 2013)

Table 2: Performance analysis between grooved wick and powdered wick in different thicknesses. (Lin & Wong 2013)

Thickness	Wick Type	Q_{max} (W)	R_0 (°C/W)	Reasons
6 mm	Grooved	40	0.65	Minimum restriction of flow with stable liquid return.
	Powdered	42	0.60	Enhanced capillarity reduces R0
3 mm	Powdered	36	0.70	Improved thermal efficiency and less clogging (risk of clogging <3 mm)
	Grooved	35	0.72	Moderate capillary action.
2.5 mm	Grooved	28	0.85	Powdered gets severely clogged, but grooved gets by
2.0 mm	Grooved	18	1.1	Only the grooved wick is still operational.

Considering key performance limiting phenomena such as condenser clogging, evaporator dryout, and condenser liquid retention losses, the selection between grooved and powdered (sintered) wicks is based on the specific thermal and geometric constraints of the required application. In the context of battery thermal management systems (BTMS), where compactness, reliability, and uniform temperature distribution are critical—both wick types offer unique advantages.

The experimental research by Lin and Wong 2013 shows (Table 2) that sintered or powdered wicks' improved capillary pumping allows them to operate best in thicker geometries (≥6 mm), attaining Q_{max} = 42 W and R_o = 0.60 °C/W. But when the whole heat pipe is flattened to less than 2.5 mm, powdered wicks lose a lot of their performance because to fluid obstruction at the condenser, which makes them inefficient (Q_{max} = 0 W at 2.5 mm). In contrast, grooved wick heat pipes maintained their functionality at thicknesses as low as 2.0 mm, with Q_{max} = 18 W and R_o = 1.10 °C/W; however, dryout was triggered early by the interplay between vapor and liquid shear. The usage of flattened grooved wick heat pipes, especially down to 2.0 mm, seems like a feasible design approach because the thesis work requires thin and flat thermal solutions to fit inside constrained packaging volumes. They can be more suited for integration into Micro Heat Pipe Arrays (MHPAs), which can be employed in BTMS, due to their performance resilience under geometrical limitations.

Thus, by flattening the heat pipe up to a flat plate to fit into tight or low profile spaces with a Grooved wick type for its better performance in the least thickness, it can be a suitable option to fulfill the requirement of this thesis. Involving the flat plate with a grooved wick, the designed MHPA can be called Micro flat plate heat pipe (MFPHP).

3.4 Performance of heat pipe materials with wicked types

Heat pipe’s thermal performance is closely related to the material and wick structure selection, each of which has unique benefits and drawbacks based on the application. Copper and aluminum emerged as the most popular materials. (H. Tang et al. 2024) showed detailed evaluation of grooved, sintered, and composite wicks because of their thermal conductivity,

manufacturing feasibility, and applicability for particular applications. Table 3 depicts the primary distinction between powdered wick and grooved wick.

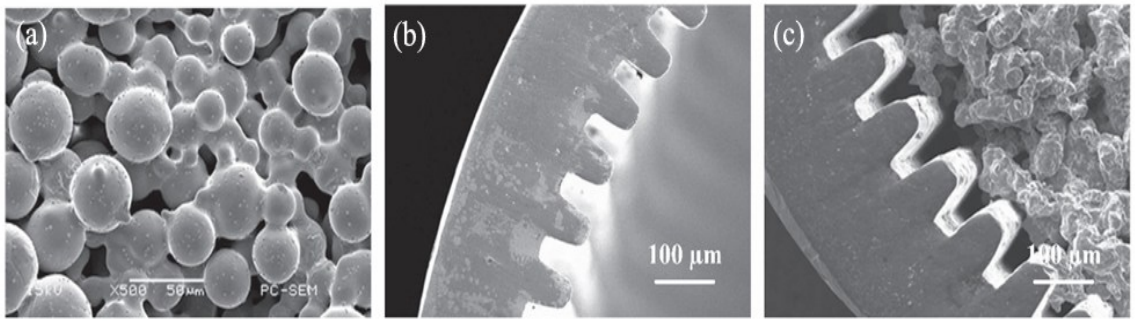

Figure 9: Heat pipe wick structures (a) Sintered/powdered wick (b) Grooved wick and (c) Composite wick. (H. Tang et al. 2024)

For high performance heat pipes, copper is still the best option, especially when combined with sintered powder wicks. These wicks have remarkable capillary pressure and permeability, which allow for effective liquid return and vapor flow. They are made by sintering copper particles into porous structures. According to (H. Tang et al. 2024), sintered copper grooved wicks outperformed other arrangements with a minimum thermal resistance (R_{min}) of 0.016 °C/W and a maximum heat transmission capability (Q_{max}) of 200 W. This is explained by the high surface area of the porous structure working in concert with the grooves' capacity to separate the liquid and vapor phases and reduce interference. Copper is perfect for high heat flux applications like CPUs and power electronics because of its excellent thermal conductivity (about 400 W/m·K), which further improves heat spreading. Copper wicks have been further refined by sophisticated methods such as laser processing and 3D printing, which have added micro/nano textured surfaces or hybrid structures (such as grooves with sintered layers) to increase capillary action. For instance, 3D printed copper wicks including fins and microgrooves demonstrated their capacity to withstand severe thermal loads by achieving a critical heat flow of 290 W/cm² in subcooled boiling. Figure 9 shows the microscopic structures in powdered wick, grooved wick, along with hybrid wick.

Despite its lower heat conductivity (≈200 W/mK), aluminum is preferred for lightweight and cost sensitive applications, such as portable electronics and aerospace. Made by milling or laser processing, grooved aluminum wicks provide dependable performance with moderate Q_{max} values (150 W for V shaped grooves, for example) and thermal resistance as low as

0.055 °C/W. However, the use of sintered aluminum wicks is limited due to the complexity of sintering operations caused by aluminum's oxidation susceptibility. To mitigate this, (H. Tang et al. 2024), have explored hybrid designs, such as laser textured grooves with secondary nanostructures, which improve hydrophilicity and capillary rise. For instance, dual scale microgrooves on aluminum obtained a capillary rise height of 72.9 mm, enabling efficient anti gravity operation. Although aluminum's raw performance is inferior to that of copper, its lightweight design and corrosion resistant coatings (such as anodization) make it a promising material for flexible thermal management systems and LED cooling.

Table 3: Comparison between grooved wick and powdered wick.

Type	Sintered/powdered wick	Grooved wick
Advantages	• High capillary pressure • Ideal for situations requiring great power and anti gravity	• Quick startup • Structural stability • Suitability for passive systems
Limitations	Complex fabrication; vulnerable to detachment under vibration.	restricted capillary function in smooth grooves; improvement requires secondary texturing (such as laser induced roughness).

Although copper is heavier and more expensive, its thermal performance is unparalleled. Compared to aluminium, oxidation is less of an issue. However, aluminium needs surface treatments (such as chemical etching and anodization) to prevent oxidation and improve wettability, while being lighter and less expensive.(H. Tang et al. 2024)

Sintered copper grooved wicks are thought to be the best for high power applications since they have a peak Q_{max} of 200W and little heat resistance. While grooves guarantee vapor liquid separation, their porous structure optimizes evaporation/condensation efficiency. Once more, laser textured aluminum grooved wicks for lightweight/portable systems combine weight and performance. Dual scale microgroove designs (Q_{max} = 150W) are perfect for aerospace systems, tablets, and cellphones. (H. Tang et al. 2024)

So, above mentioned laser textured aluminum grooved wicked, including 5mm thick MHPHP, will most likely be the best option for this refrigerant based optimum battery thermal management system to satisfy the purpose of this thesis.

3.5 Heat pipes working fluid analysis

An important component of the current design's performance would be working fluids. Ammonia, Freon, cyclopentane, acetone, and n hexane are utilized as working fluids for aluminum heat pipes based on their chemical compatibility with aluminum and favorable thermophysical properties such as high latent heat, suitable vapor pressure, and low viscosity (Huang et al. 2018). However, only low temperature heat pipes can use Freon and ammonia. Figure 10 (c) depicts the working principle of micro grooved aluminum flat plate heat pipes (MFPHPs). Within sealed microchannels, the grooves serve as capillary wicks that promote the flow of a working fluid. The evaporator, adiabatic, and condenser zones are the three primary components of the basic process as previously discussed. The working fluid absorbs thermal energy and changes phases from liquid to vapor when heat is introduced to the evaporator section. Driven by the pressure gradient, the resultant vapor moves in the direction of the condenser portion, where it releases its latent heat and condenses back into liquid. Capillary action then returns the condensed liquid to the evaporator via the micro grooved capillary tubes. The system can transfer heat with great efficiency and little temperature loss because of this closed loop circulation. A greater contact surface area and

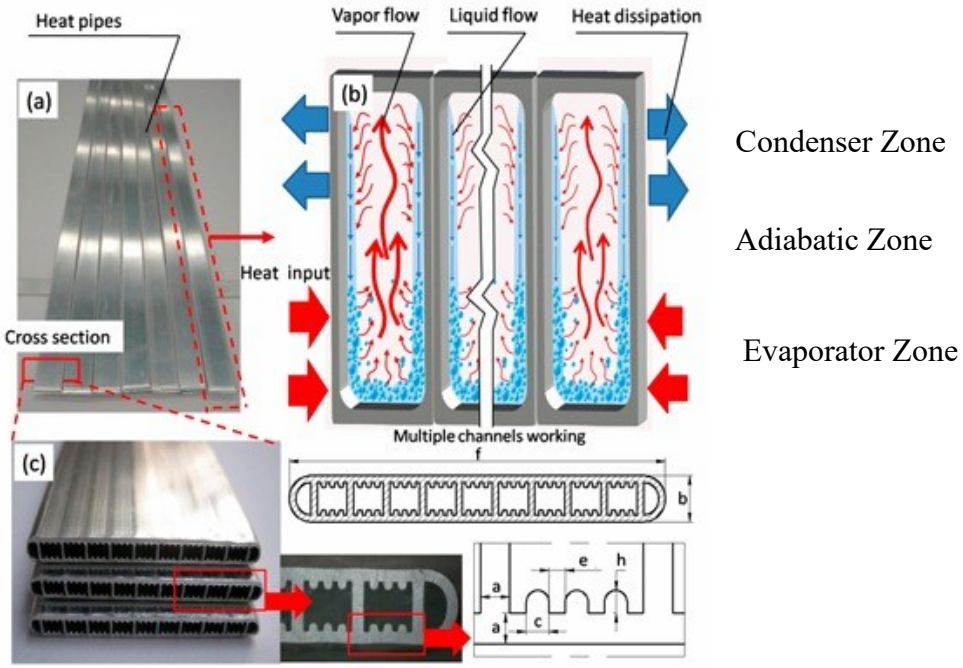

Figure 10: Geometric design and working mechanism of the Micro grooved aluminum flat heat pipes (MFPHPs) (a) Image of (MFPHP); (b) Multiple channels working principle; (c) Section view of MFPHP (Huang et al. 2018).

superior integration with planar heat sources, such as battery packs or other heat sources, are made possible by the flat plate geometry as discussed in the previous parts. The aluminum shell's inner ribs also act as thermal fins, increasing the effective evaporating area and improving lateral heat distribution. Crucially, every microchannel functions autonomously, enhancing system dependability and resilience to non condensable gases or manufacturing flaws.

Using acetone, cyclopentane, and n hexane as working fluids, Huang et al. (2018) experimented the thermal performance of micro grooved flat heat pipes (MFPHPs) with a geometrical sample shape having a thickness of 3mm, width of heat pipe is 26mm, width of the microfine is 0.35mm, a height of microfine is 0.32mm and width of microgroove is 0.25mm. Because of acetone's advantageous thermophysical characteristics, such as its higher latent heat and lower viscosity, it surpassed the others. The evaporator temperature fluctuated between 60°C and 120°C during the controlled trials, which used heat inputs ranging from 10 W to 60 W. A water cooling system with a constant flow rate was used to keep the condenser portion at about 25 °C, guaranteeing constant heat dissipation during the testing. Acetone's high latent heat of vaporization improved heat absorption during evaporation, while its low viscosity reduced flow resistance in the microgrooves. Its strong surface tension (shown by a high Laplace number) guaranteed effective capillary driven liquid return from the condenser to the evaporator, and its high thermal conductivity enhanced heat diffusion. In comparison to cyclopentane and n hexane, these characteristics enabled acetone to achieve reduced thermal resistance, improved temperature uniformity, and faster start up times. The cyclopentane and n hexane experienced instability at high heat loads and decreased heat transfer efficiency due to thicker liquid layers in the condenser and increased viscous friction.

Figure 11 visualizes the working of liquid films where heat absorbed at the evaporator vaporizes the working fluid, which then moves to the condenser, releases heat and condenses back into liquid. This is how the working fluid functions in micro grooved heat pipes. Surface tension drives capillary action through the microgrooves, which brings the liquid back to the evaporator. Because of its strong capillary forces, acetone prevented dry out in the evaporator and maintained thin, uniformly dispersed liquid coatings in the condenser, which decreased thermal resistance.

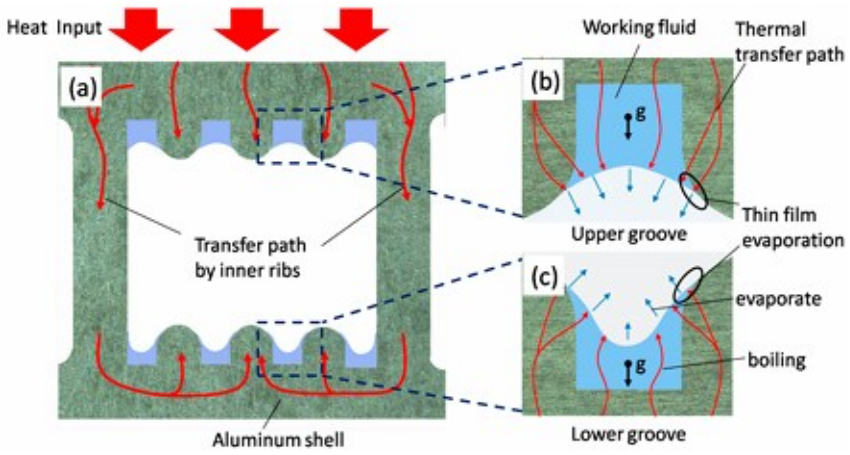

Figure 11: Schematic showing the distribution of liquid films and the heat transfer path inside a channel when heated from the upper surface (a) view of the entire cross section of the channel; (b) distribution of liquid in the upper groove; (c) distribution of liquid in the bottom groove. (Huang et al. 2018)

A heat pipe's inclination angle has a major impact on its thermal performance because it alters the interaction between capillary driven fluid return and gravity driven liquid drainage. Gravity offers little help at low inclination degrees (nearer horizontal), therefore the system must rely almost exclusively on capillary action from the microgrooves to return condensed liquid to the evaporator. If capillary forces are not enough to overcome vapor shear forces or viscous resistance, especially at high heat loads, this could result in evaporator dry out. On the other hand, excessive gravitational drainage at steep angles (such as >75°) can result in flooding in the condenser and liquid pooling in the evaporator, thickening the liquid film and raising thermal resistance. Because they ensure enough capillary driven distribution while balancing gravity's function in facilitating liquid return, the study by (Huang et al., 2018) revealed that intermediate angles, such as 25° to 75° were ideal. Because of their higher viscosity and lower capillary action, cyclopentane and n hexane performed better at steeper angles (up to 75°) than acetone based heat pipes, which only achieved negligible thermal resistance at 25° to 45°. This balance is reflected in the suggested volumetric fraction criterion (74% ± 7%), where the volumetric fraction is defined as the ratio of the total volume of the microgrooves in the condensation and adiabatic sections of the heat pipe to the volume of working fluid present in those sections. Ideal angles guarantee that there is enough liquid in the adiabatic and condenser sections to avoid dry out while preventing too much fluid

could overflowing the evaporator. By balancing capillary and gravitational forces and taking into account the characteristics of the working fluid and the groove geometry, the ideal inclination angle is established for real world applications such as solar collectors to enable effective heat transfer. When the ideal inclination angles with various working fluids, i.e., changing from 25 to 75, are significantly altered, the $\alpha_{c,a}$ in Figure 12(a) varies somewhat from 66.5% to 70.8%. Figure 12(b) shows a similar pattern for the different heat loads on the acetone heat pipe. It is evident from the experimental data that the liquid volumetric fractions have a substantial relationship with the ideal inclination angle. The chosen ideal volumetric fractions seem to have a mean value of 74%, with a 7% variation.

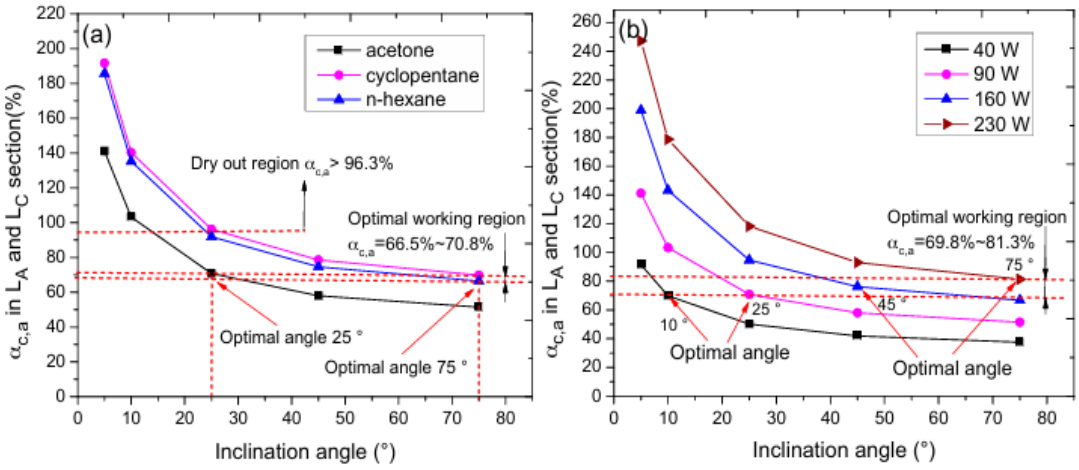

Figure 12: The volumetric fraction in adiabatic and condensation wicks as a function of inclination angle for (a) various working fluids under a 90 W heat load and (b) various acetone MFPHPs heat loads. (Huang et al. 2018)

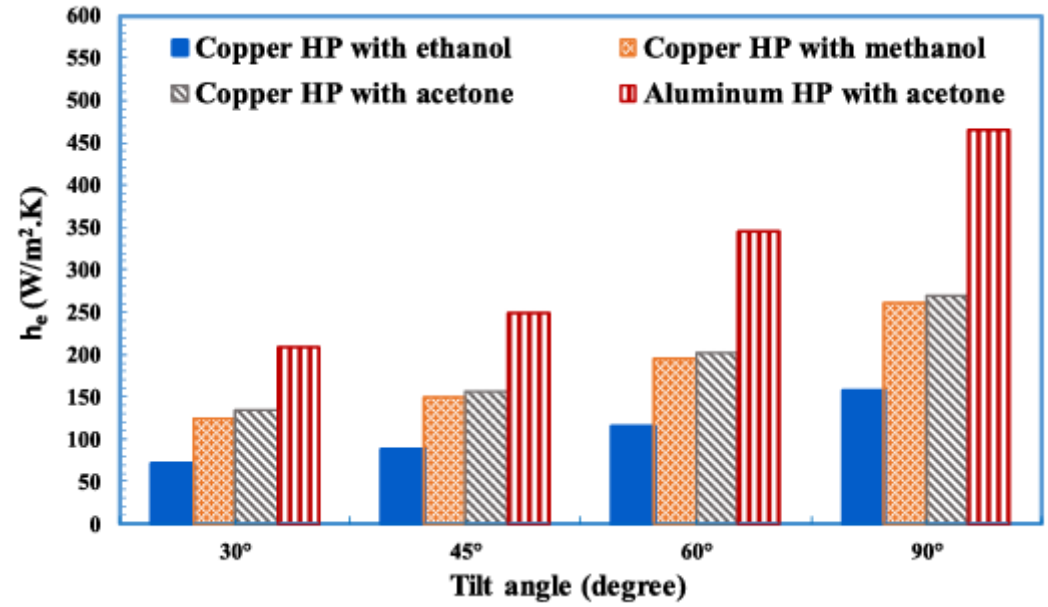

(a)

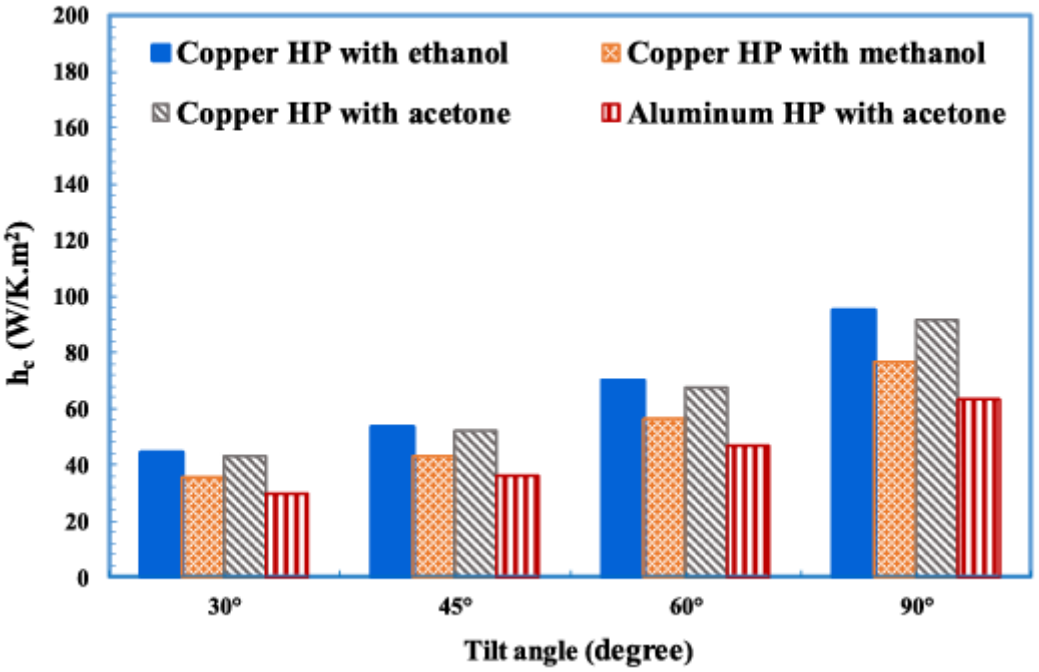

(b)

Figure 13: (a) The effect of tilt angles on the evaporator heat transfer coefficient for four distinct heat pipe types at a 30% filling ratio and a 60 W input power; (b) The effect of tilt angles on the condensation heat transfer coefficient for four distinct heat pipe types at a 30% filling ratio and a 60 W input power. (A.M. Al Jubori and Q.A. Jawad et al. 2022).

The thermal performance of copper and aluminum heat pipes (HPs) using acetone, methanol, and ethanol as working fluids for applications involving chilled containers is experimentally assessed by A.M. Al Jubori and Q.A. Jawad et al. 2022 has shown in Figure 13. The condenser was chilled with dry ice (-78°C) and tested under different input powers (5-60 W), tilt angles (30°-90°), and filling ratios (15 and 30%). Because of acetone's low viscosity, high latent heat, and compatibility with copper, the results revealed that copper HPs with acetone outperformed ethanol and methanol and obtained the lowest thermal resistance (2.2 K/W) at 30% filling ratio, 60 W input power, and vertical orientation (90°). Aluminum HPs showed competitive performance (2.6 K/W) but were limited to acetone because the material was incompatible with ethanol and methanol. By maximizing capillary action and gravity assisted fluid return, vertical orientation reduced heat resistance, and higher filling ratios (30%) guaranteed enough fluid for evaporation without flooding. In order to design effective HPs for low temperature applications like refrigerated transport, where copper-acetone configurations perform well under high heat loads, the study emphasizes the significance of material compatibility (such as aluminum's limitations with specific fluids) and operational parameters (tilt angle/inclination angle, filling ratio).

4 Functional Design and Implementation Strategy

4.1 Geometrical Design Analysis and Implementation

For the initial approach, a 21700 Li-ion battery model with 70mm of height and 21mm of width (from Table 4) has been considered. Choosing the right lithium-ion cell configuration is crucial for electric vehicles (EVs), particularly when they operate in harsh climates and have high rate charge/discharge cycles. This is because the configuration has a direct impact on heat generation (heat sink/source), thermal distribution, and the efficiency of the battery thermal management system (BTMS). An ideal setup guarantees consistent temperature profiles, reduces heat stress, and extends battery life and safety in difficult operating conditions. The chosen battery cell for this thesis has to have a large surface area, a high energy density and good thermal stability that allows micro flat plate heat pipes (MFPHPs)

to be directly integrated. A higher energy density reduces the total number of cells required, lowering system volume and complexity, while a larger surface area facilitates more effective thermal contact with the MFPHPs. The 21700 cylindrical lithium-ion cell has been chosen as the case study for the thermal management system designed for this thesis because of its applicability and suitability for cutting edge cooling techniques. It is an ideal choice for integration with the suggested micro flat plate heat pipe (MFPHP) based system because of its well balanced high energy density, structural stability, and standardized form factor. In order to assess the performance of the MFPHP system under practical battery configurations, the cylindrical shape offers reliable thermal boundaries and enough surface area for efficient heat transmission..(AMS Battery 2021)

Table 4: Comparison between 21700 and 18650 Li-ion cell models. (AMS Battery 2021) (Q. Wu et al. 2023)

Specification	**21700 Cell**	**18650 Cell**
Diameter (Tentative)	21.0mm (± 0.2mm)	18.6mm (± 0.2mm)
Length (Tentative)	70.0mm (± 0.2mm)	65.2mm (± 0.2mm)
Nominal Voltage	3.6 – 3.7 volts	3.6 – 3.7 volts
Capacity	4000-5000mAh	2600-3500mAh
Gravimetric Energy Density	250-300 Wh/kg	200-260 Wh/kg
Volumetric Energy Density	700-750 Wh/L	600-650 Wh/L
Continuous Discharge Rates	10- 15A (Standard) 30- 45A (High-drain)	5- 10A (Standard) 15- 30A (High-drain)
Pulse Discharge Capability	Up to 70-100A	Up to 40-60A
Longevity	600-1500 cycles to 80% capacity	300-1000 cycles to 80% capacity

By conforming to the cylindrical curve of the battery, the MFPHPs, which are constructed with exact geometric characteristics (70 mm length and 5 mm width) to ensure the same height of the battery model. The heat source is fixed (21mm) and MFPHP surrounds the battery half of almost the battery's diameter (21mm ÷ 2) = 10.5mm. If the MFPHP continues straight, it can only touch some portion of each of the batteries. To mitigate this, MFPHP has considered in wavy shape to get contact with half of the surface area (10.5mm) and continues to the parallel alignment of the batteries. As the material of the MFPHP is Aluminum, as discussed in Section 3.5, which is lighter in weight and flexible. Continuing the exact shape with Aluminum, especially when two curves are merging together. This

situation can create variable MFPHP contact areas with the batteries. Also, when EV runs, the vibration created by the vehicle can dislocate the battery from the MFPHP's contact area, which will not only decrease overall efficiency and performance of the MFPHP also escape from the main purpose of the system, which is temperature control. Also, uncontrolled temperature of a few batteries in a pack can create thermal unstability, which might cause thermal runaway too. To mitigate this situation, a graphite pad interface (thermal conductivity:300-500W/m·K) has been positioned to ensure ideal thermal contact between each battery cell and the MFPHP contact surface (C. Wang et al., 2025). By reducing interfacial resistance, this pad can facilitate effective heat transmission from the battery surface to the heat pipe's evaporator section. (G. Chen et al. 2020) has shown the thermal performance of flat plate heat pipes with a specific geometrical shape. Based on the experimental investigation of working fluids by(Huang et al. 2018), along with the thermal performance analysis conducted by (G. Chen et al. 2020), optimal results were achieved using a micro grooved structure with consistent axial parameters: 0.35 mm fin width, 0.25 mm groove width, and 0.32 mm fin height. Figure 14 shows 3D sample of a flat plate grooved heat pipe with similar parameters. To maintain these experimentally proven performances, the internal geometry of the microgroove structure was kept the same in the present study**.** Also, as per (Huang et al. 2018) the thermal conductivity heat pipe relies on the volume of the connected layer of the heat pipe. So the diameter of the MFPHP is considered 1mm on each side ((5mm -3mm) = 2mm; 1 mm each side).

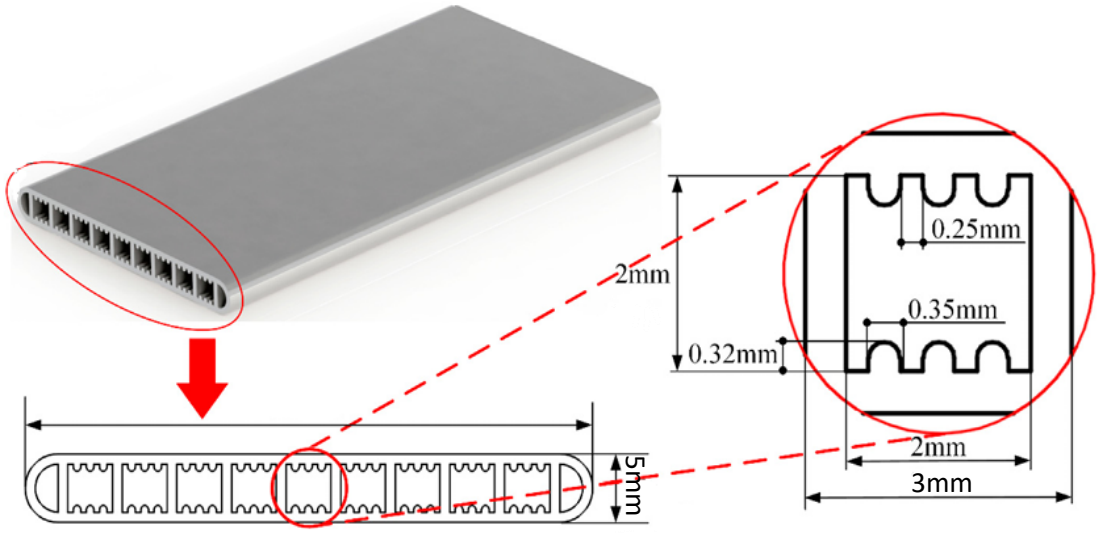

Figure 14: Proposed schematic design of wavy micro-grooved aluminium flat plate heat pipe (MFPHP) array. (G. Chen et al. 2020)

A single microchannel has been initially examined in this work, where the measured microchannel is 0.25 mm wide and 0.32 mm high. With a fin width of 0.35 mm and a wall thickness of 0.50 mm, the aluminium substrate thickness is considered to be constant (following G. Chen et al. 2020). The cross section of the microchannel under investigation is depicted in Figure 15, and Table 5 provides a summary of the microchannel's dimensions.

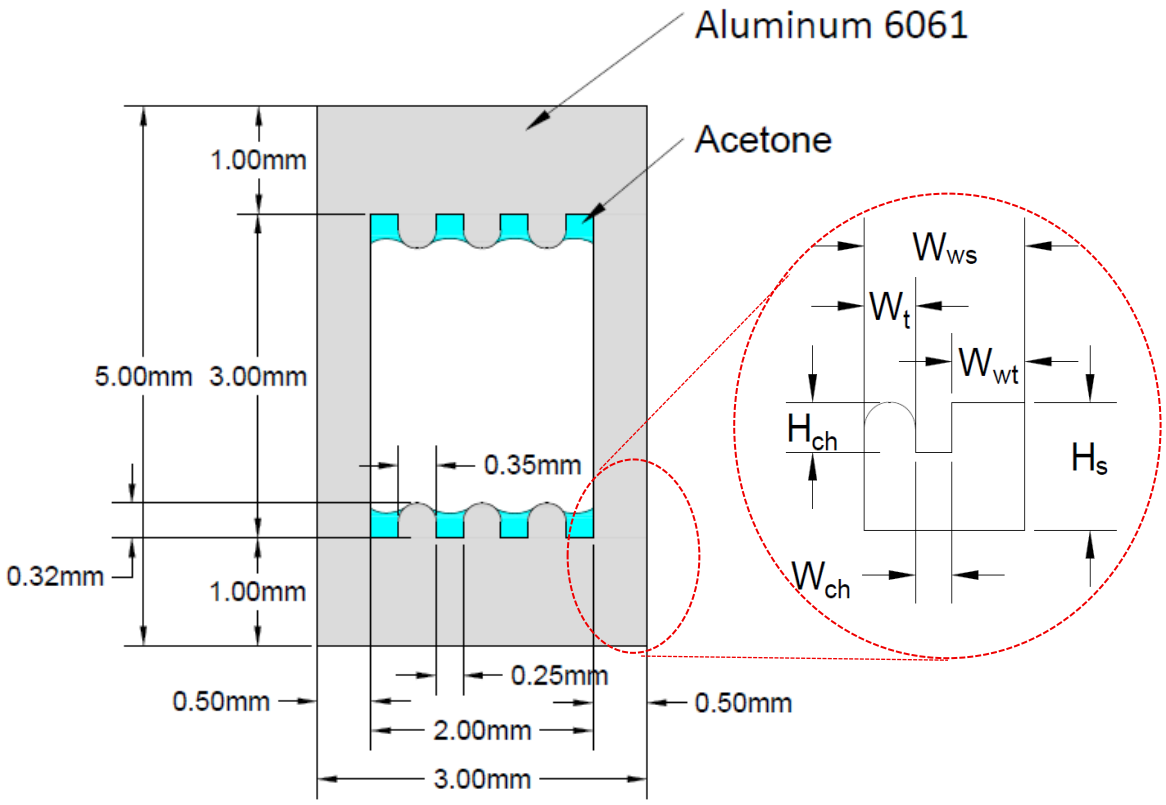

Figure 15: The cross section of the studied single channel.

Table 5: Dimensions of the single channel.

H_{ch} (mm)	Height of each channel	0.32
W_{ch} (mm)	Width of each channel	0.25
W_t (mm)	Channel fin width	0.35
W_{wt} (mm)	Wall thickness	0.50
H_s (mm)	Distance from channel fin to bottom wall	1.32

The wavy geometries were generated based on the trigonometric profile of $y = A\,\mathrm{Cos}(2\pi x/\lambda)$ where A is the wavy amplitude, and λ is the wavelength. The top view of a portion of the

channels is shown in Figure 16, and Table 6 provides the geometrical specifications of the microchannel.

According to Ghorbani et. al (2022), geometries with a higher amplitude to wavelength ratio have a smaller radius of curvature, a higher Dean number, and improved heat transfer due to transverse flow (secondary flow) amplification. According to the performance evaluation criterion (PEC) by Ghorbani et. al (2022), the wavy example with an amplitude of 250 μm and a wavelength of 2500 μm ($\frac{A}{\lambda} = 0.1$) is the best shape in the range under study from a thermal hydraulic perspective. So, considered similar to a larger amplitude to wavelength ratio with a wavelength of 105 mm. The projected wavy heat pipe's channel count is presented in Table 6.

Table 6: Number of channels on the proposed wavy heat pipe.

A	Amplitude of the channel's waviness	10.5 mm (radius of 21700 battery)
λ	Wavelength of the channel's waviness	105 mm
n_1	Number of channels on each side wall	4
n_2	Number of channels on each acting individual heat pipe	8
n	Number of acting individual heat pipes at designed heat pipe	23

R_c is the radius of curvature that is given by Equation (1) (Ghorbani et. al 2022).

$$R_c = \frac{(1+(\frac{dy}{dx})^2)^{3/2}}{|\frac{d^2y}{dx^2}|} \qquad (1)$$

As previously stated, the trigonometric profile of $y = A\text{Cos}(2\pi x/\lambda)$, where A is the wavy amplitude and λ is the wavelength, is used to construct wavy geometries. Therefore, to compute the radius of curvature, R_c

$$dy/dx = (-\frac{2\pi A}{\lambda}) \text{ Sin } (\frac{2\pi x}{\lambda}) \qquad (2)$$

$$d^2y/dx^2 = - (\frac{2\pi}{\lambda})^2 \text{ A Cos } (\frac{2\pi x}{\lambda}) \qquad (3)$$

In this work, R_c is computed at the extremum of $y = A\text{ Cos}(2\pi x/\lambda)$, which ultimately leads to the maximum Dean number and lowest R_c. Additionally, x is a multiple of λ/2 at the extremum position, therefore, $\text{Sin}(2\pi x/\lambda)$ is zero, while $\text{Cos}(2\pi x/\lambda)$ is equivalent to 1. So, from Equations (2) and (3)

$$dy/dx = 0$$

$$d^2y/dx^2 = -37.5987$$

So, from Equation (1)

$$R_c = 0.02659 \text{ m} = 26.59 \text{ mm}$$

The longitudinal arc length over one wavelength ($x \in [0, \lambda]$) is

$$L_{1\lambda} = \int_0^{\lambda} \sqrt{1 + (\frac{dy}{dx})^2}\ dx$$

$$= \frac{\lambda}{2\pi} \int_0^{2\pi} \sqrt{1 + k^2\ sin^2\theta}\ d\Theta$$

Where,

$$k = \frac{2\pi A}{\lambda},\ \Theta = \frac{2\pi x}{\lambda}$$

Although complete elliptic integrals (elliptic integrals of the second sort with an imaginary modulus) can be used to define the integral, a short series expansion is more precise and understandable for engineering applications.

So, in the Series expansion (rapidly convergent for moderate slope)

Using $\sqrt{1+u} = 1 + \frac{1}{2}u - \frac{1}{8}u^2 + \ldots\ldots$ And averaging $\sin^2$ and $\sin^4$ over a period provides

$$\frac{L_{1\lambda}}{\lambda} = 1 + \frac{k^2}{4} - \frac{3k^4}{64} + 0\ (k^6) \qquad (4)$$

As, $k = \frac{2\pi A}{\lambda} = 0.62832$

So, from Equation 4,

$$\frac{L_{1\lambda}}{\lambda} = 1.091395$$

$$L_{1\lambda} = 114.60 \text{ mm}$$

So, the geometrical characteristics of the wavy channel have been illustrated in Table 7.

Table 7: characteristics of the wavy microchannel's geometry.

A (mm)	λ (mm)	$\frac{A}{\lambda}$	R_c (mm)	$L_{1\lambda}$ (mm)
10.5	105	0.1	26.59	114.60

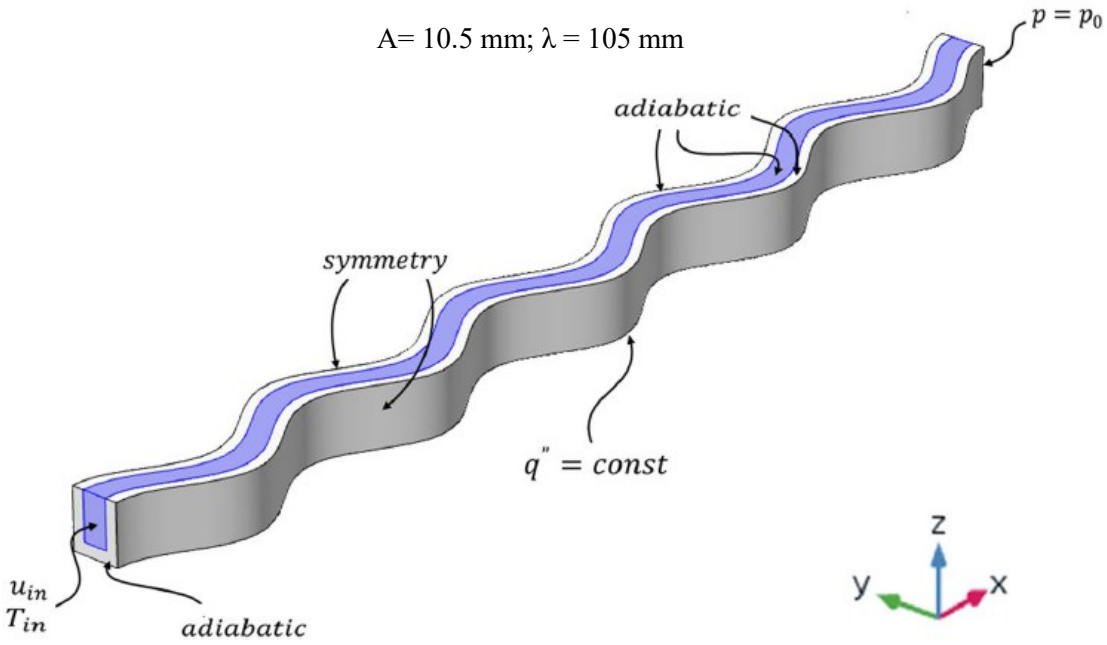

Figure 16: Wavy channel diagram with the desired boundary conditions. (Ghorbani et. al 2022).

4.2 Boundary Condition:

The boundary conditions are stated as follows: the pressure at the outlet is given as atmospheric pressure, and the fluid velocity and temperature are assumed to be constant at the input. In the meantime, a steady heat flux is applied to the microchannel's bottom surface, and the boundary condition at the side walls is considered symmetrical. The other exterior surfaces of the heat sink substrate that are compatible with the actual scenario of appropriate

isolation are subjected to the adiabatic boundary condition. The solid and fluid temperatures are assumed to be equal at the contact, and the heat flux is likewise taken to be continuous. The velocity on the microchannel walls is zero under the no-slip condition. The boundary conditions are presented in Table 8 and Figure 16. Where, $T_{f,in}$ is the fluid inlet temperature, p0 is the air pressure, u, v, and w are the components of the velocity vector in the x, y, and z directions, q" is the heat flux applied to the substrate's bottom surface, and uin is the fluid

Inlet velocity. The solid and fluid temperatures are T_s and T_f. The direction perpendicular to the surface is denoted by n.

Table 8: Thermodynamic Boundary Conditions.

At the inlet	**At outlet**	**At the substrate's bottom surface**	**At the fluid-solid interface**	**Other outer surfaces**
$u = u_{in}$; $v = w = 0$; $T = T_{f,in}$	$p = p_0$	$q'' = -k_s \frac{\partial T_s}{\partial n} = \text{const}$	$u = v = w = 0$; $T_s = T_f$; $k_s \frac{\partial T_s}{\partial n} = k_f \frac{\partial T_f}{\partial n}$	$q'' = -k_s \frac{\partial T_s}{\partial n} = 0$

4.3 Numerical Modelling:

The hydraulic diameter of the channel is defined by,

$$D_h = \frac{4 \times Ac}{Pc} \qquad (5)$$

Here, A_c is the cross-sectional area of a single channel, and P_c is the perimeter of the microchannel cross-section.

So, $A_c = W_{ch} \times H_{ch} = (0.25 \times 0.32)\ mm^2 = 0.08\ mm^2$.

Again, $P_c = 2(W_{ch} + H_{ch}) = 2 \times (0.25 + 0.32) = 1.14$ mm.

Now, from Equation (5), the hydraulic diameter of a single channel is = $(4 \times 0.08\ mm^2)/1.14mm = 0.2807$ mm.

Table 9: Thermophysical characteristics of the working fluid and substrate material.

Properties	Liquid acetone (25 °C, 1 bar)		Reference
Fluid density	ρ_f (kg/m^3)	784.6	Engineering Toolbox (2023)
Specific heat of fluid	Cp_f (J/kgK)	2169	NIST Chemistry WebBook (2023)
Thermal conductivity of fluid	k_f (W/mK)	0.153	Huber (2016, NIST TRC data set)
Fluid dynamic viscosity	μ_f(kg/ms)	0.000316	NIST Chemistry WebBook (2023)
Surface tension of fluid	σ (N/m)	0.0236	Engineering Toolbox (2023)
Aluminum 6061 (25 °C, 1 atm)			
Solid density	ρ_s (kg/m^3)	2700	TechSteel (2023)
Specific heat of fluid	Cp_s (J/kgK)	896	MatWeb (2023)
Thermal conductivity of fluid	k_s (W/mK)	167	MatWeb (2023)

A grooved microchannel heat pipe's maximum operating length is determined by the capillary limit, which stipulates that the maximum capillary pressure produced by the wick or groove structure must be larger than or equal to the system's overall pressure losses (Faghri, 1995; Reay & Kew, 2006). This circumstance can be expressed as

$$\Delta P_{cap} \geq \Delta P_l + \Delta P_v + \Delta P_g, \qquad (6)$$

where ΔP_{cap} is the available capillary pressure, and the other terms represent the pressure losses due to liquid flow (ΔP_l), vapor flow (ΔP_v), and gravity (ΔP_g), respectively. Gravity (ΔP_g), and vapor pressure drop (ΔP_v), are neglected in this analysis due to the complexity of the analysis and relatively low values, as ΔP_l is the dominant one (Reay & Kew, 2006), which concentrates on the liquid pressure drop (ΔP_l) in the microchannels serving as the wick.

According to the Laplace–Young equation for meniscus pressure difference, the capillary pressure is,

$$\Delta P_{cap} = \frac{2 \times \sigma \times \cos\theta}{r\mathrm{eff}} \qquad (7)$$

Here, σ (N/m) is the surface tension of the working fluid (acetone). r_{eff} is the effective capillary radius and θ is the contact angle of wetting. For the Meniscus contact of fully wetting ($\cos\theta = 1$). So, the Equating (7) can be further expressed as

$$\Delta P_{cap} = \frac{2 \times \sigma}{r\mathrm{eff}} \qquad (8)$$

The Young-Laplace equation provides the maximum capillary pressure. In a rectangular groove, the hydraulic radius of the channel approximates the effective capillary radius for a perfectly wetting fluid (acetone on aluminium, $\theta \approx 0°$, $\cos\theta = 1$).

Now, the effective capillary radius is

$r_{eff} = \frac{Dh}{4}$ = (0.2807/4) mm = 0.070175mm.= 7.0175×10^{-5} m.

So, from Equation (8) and Table (9)

$$\Delta P_{cap} = \frac{2 \times 0.0236}{7.0175\times 10^{-5}}$$

$$= 672.60 \text{ Pa}$$

The Darcy–Weisbach relation can be used to express the viscous pressure drop for the liquid return flow in microchannels as

$$\Delta P_l = f \times \frac{L_{ch}}{D_h} \times \frac{\rho\, u_{avg}^2}{2} \qquad (9)$$

where f is the friction factor, L_{ch} is the length of the effective liquid flow, and D_h is the hydraulic diameter, while u_{avg} is the average longitudinal velocity of liquid. According to G. Xia et al. 2011, the friction factor is one of the main hydraulic performance indicators that is evaluated by

$$f = \frac{2 \times \Delta Pl \times D_h}{\rho \times L_{ch} \times u_{avg}^2} \qquad (10)$$

Also, the Reynolds number (Re) can be defined by

$$Re = \frac{\rho \times u_{avg} \times D_h}{\mu} \qquad (11)$$

From Equations (9) and (10), the maximum permitted length of a heat pipe can be expressed by substituting this into the relation above and equating it with the capillary pressure,

$$L_{max} = \Delta P_{cap} \times \frac{2 \times \rho_f \times D_h^3}{f \times Re^2 \times \mu^2} \qquad (12)$$

The Laplace–Young equation, the Darcy–Weisbach pressure drop model, and the traditional capillary limit formulation all immediately lead to this result (Faghri, 1995; Reay & Kew, 2006; Dunn & Reay, 2014). In depth studies of friction factor correlations for microchannels with sinusoidal and wavy geometries have been conducted by Shah & London (1978) and

Sui et al. (2010). Faghri and Khrustalev also provide similar derivations for grooved microchannel geometry (1996).

Based on the range of the Reynolds number, the flow in this work is regarded as laminar and incompressible. Interestingly, Kandlikar et al. 2013 state that the laminar to turbulent transition in microchannels happens at about 2300 Reynolds numbers. Furthermore, Sui et al. (2011) conducted a well known experimental work that examined the wavy microchannel heat sink in the Re = 300 to 800 range and clarified that the flow regime is laminar in both straight and wavy microchannels. Also, Khoshvaght-Aliabadi et al. 2017 researched the enhancement of laminar forced convection cooling in a wavy heat sink in the range of Re = 100 to 900 and claimed that the flow regime is laminar. Similarly, numerous references demonstrate that the Reynolds number for the large scale and micro scale transitions does not differ much (Ghorbani et. al 2022). Thus, the current study's flow regime (Re = 100 to 900) is likewise regarded as laminar. The following other assumptions are considered: (1) constant solid and fluid properties (because of the small temperature changes); (2) negligible gravitational force; (3) neglected viscous dissipation; (4) neglected heat loss between the ambient and the microchannel; and (5) neglected natural convective and radiative heat transfer.

The dimensionless variable known as the friction factor (*f*) describes the pressure drop in a flow channel caused by viscous processes. Because of flow separation brought on by the periodic curvature and secondary flows like Dean vortices, wavy microchannels have a higher friction factor than straight channels. A common method for measuring this improvement is the correlation from Rush et al. 1999.

$$\frac{f_{wavy}}{f_{straight}} = [\ 1+ (\frac{A}{\lambda})^{1.37} \times (\frac{2\ D_h}{\lambda}\ \mathrm{Re})^{0.897}]^{0.718} \qquad (13)$$

Where, f_{wavy} is the friction factor for the wavy channel, f_{straight} is the friction factor for an equivalent straight channel, A is the amplitude of the channel's waviness, λ is the wavelength of the waviness, D_h is the hydraulic diameter of the channel and Re is the Reynolds number.

For laminar flow in ducts with different cross sections, the formula f×Re = constant, which is a fundamental concept in fluid mechanics. This book by Shah & London (1978) is the premier source for experimental, numerical, and analytical information on heat transfer and

flow in ducts of almost any shape. It offers comprehensive tables for the product f. Re for rectangular ducts as a function of the aspect ratio α. Where, α = b/a ≤ 1 with a and b being the sides of the rectangular shape. From Figure(15) and Table (5), H_{ch} = 0.32mm and W_{ch} = 0.25mm, where the longer side is 0.32 mm, the shorter is 0.25 mm. Therefore, α = (0.25/0.32) = 0.78125.

The product f·Re is constant for fully developed laminar flow in rectangular ducts and solely depends on the duct aspect ratio. The constant is 59.5 for an aspect ratio of α = 0.78 (Shah & London, 1978; Kandlikar et al. 2013; G. Xia et al. 2011).

So,

$$f_{\text{Straight}} \times \text{Re} = 96\,(1 - 1.3553\alpha + 1.9467\alpha^2 - 1.7012\alpha^3 + 0.9564\alpha^4 - 0.2537\alpha^5)$$

$$f_{\text{Straight}} = \frac{57.624}{Re}$$

Now, From Equation (13)

$$f_{wavy} = [\,1 + (\frac{A}{\lambda})^{1.37} \times (\frac{2\,D_h}{\lambda}\,\text{Re})^{0.897}]^{0.718} \times \frac{59.5}{Re} \qquad (14)$$

Using Equation 11, for the values of Reynolds numbers 100 to 900, the friction factor for both straight and wavy geometry has been calculated and presented in Table 10.

Table 10: Friction factor estimation for current single channel straight and wavy geometry.

Re	**A (m)**	**λ (m)**	**D_h (m)**	**f_{Straight}**	**$(A/\lambda)^{1.37}$**	**$(2 \times Dh \times Re)/\lambda)^{0.897}$**	**f_{wavy}**
100	0.0105	0.105	0.0002807	0.595	0.042658	0.570283162	0.6053575
200	0.0105	0.105	0.0002807	0.2975	0.042658	1.061975396	0.307116
300	0.0105	0.105	0.0002807	0.1983333	0.042658	1.527806363	0.2075312
400	0.0105	0.105	0.0002807	0.14875	0.042658	1.97759958	0.1576564
500	0.0105	0.105	0.0002807	0.119	0.042658	2.415831517	0.1276826
600	0.0105	0.105	0.0002807	0.0991667	0.042658	2.845065181	0.1076673
700	0.0105	0.105	0.0002807	0.085	0.042658	3.266957546	0.0933473
800	0.0105	0.105	0.0002807	0.074375	0.042658	3.682665449	0.0825897
900	0.0105	0.105	0.0002807	0.0661111	0.042658	4.093040858	0.0742088

Table 11: Operating length estimation for the current single channel wavy geometry

Re	**ρ (Kg/m3)**	**D_h (m)**	**μ(kg/ms)**	**U_{avg} (m/s)**	**U^2avg (m^2/s^2)**	***f* wavy**	**ΔP_{cap} (Pa)**	**L_{max} (mm)**
100	784.6	0.0002807	0.000316	0.14348	0.02059	0.605358	672.6	38.616802
200				0.28696	0.08235	0.307116		19.029429
300				0.43044	0.18528	0.207531		12.515907
400				0.57393	0.32939	0.157656		9.2673724
500				0.71741	0.51467	0.127683		7.3234659
600				0.86089	0.74113	0.107667		6.0311728
700				1.00437	1.00876	0.093347		5.1108153
800				1.14785	1.31757	0.08259		4.4226476
900				1.29133	1.66755	0.074209		3.889086

Here, from Table 11, the L_{max} is too small to fulfil design purposes. With the existing L_{max} the acetone will dry out very soon. Table 11, illustrates the operating length with maximum capillary pressure related to the hydraulic diameter (D_h). where, D_h is related to the height of each channel (H_{ch}) and the width of each channel (W_{ch}). On the other hand, f_{wavy} the friction factor (from Table 10) for the wavy channel relies on the aspect ratio α = (0.25/0.32) = 0.78125. So, taking the constant aspect ratio. The new proposed height of each channel and the width of each channel with an unchanged Channel fin width (W_t). The upgraded dimensions and properties can be depicted in Table 12 and Figure 17.

Table 12: Dimensions and properties of the upgraded single channel.

$H_{ch,new}$ (mm)	New height of each channel	1.1
$W_{ch,new}$ (mm)	New width of each channel	1.4
W_t (mm)	Channel fin width	0.35
W_{wt} (mm)	Wall thickness	0.5
$H_{s,new}$ (mm)	New distance from channel fin to bottom wall	1.6
$D_{h,new}$ (mm)	Hydraulic diameter of the new channel	1.232
$r_{eff,new}$ (mm)	Effective capillary radius of the new channel	0.308
$\Delta P_{cap,new}$ (pa)	The maximum capillary pressure of the new channel	153.247
n_1	Number of channels on each side wall	3
n_2	Number of channels on each acting individual heat pipe	6
n	Number of acting individual heat pipes at the designed heat pipe	12

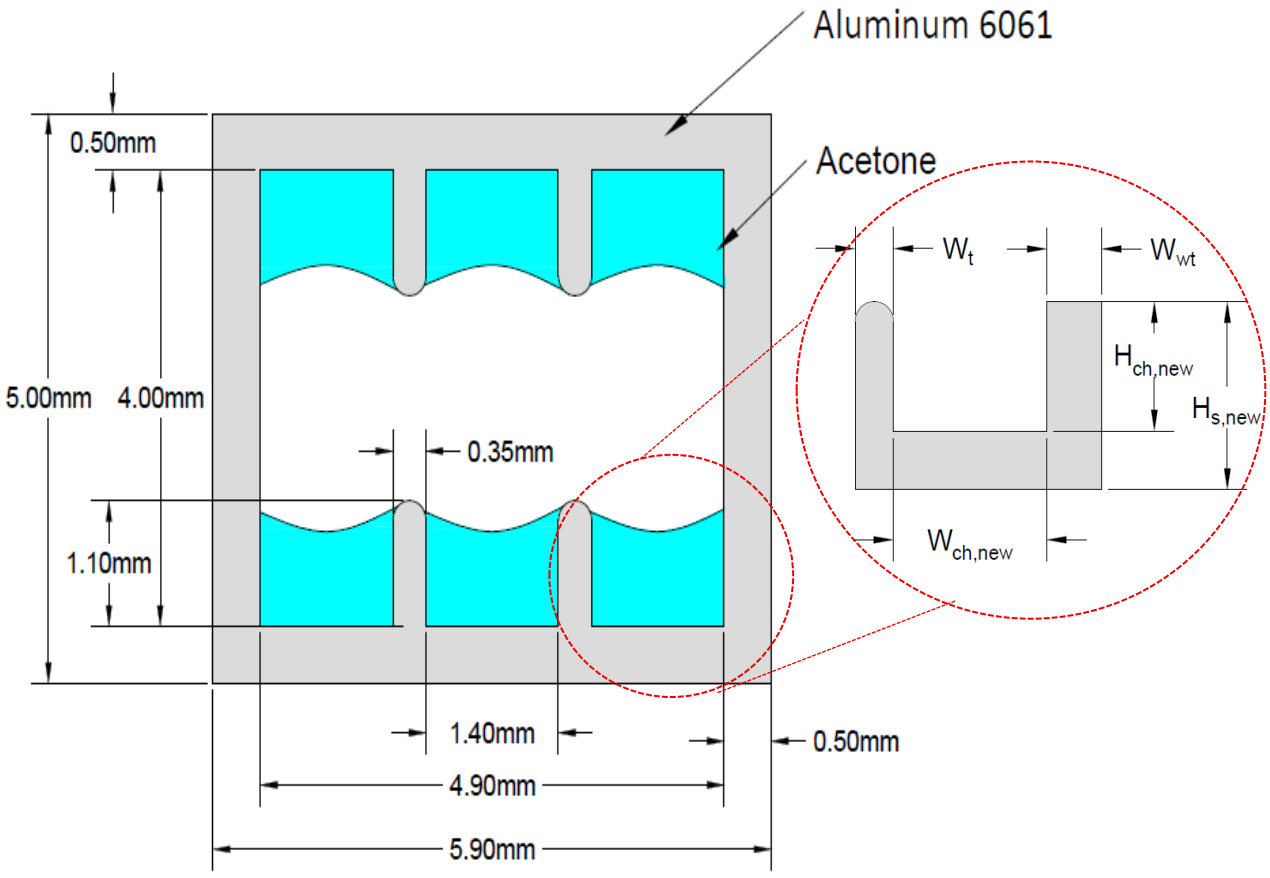

Figure 17: The cross section of the upgraded single channel.

Table 13: New friction factor estimation for the current single channel wavy geometry.

Re	A (m)	λ (m)	D_h (m)	$f_{Straight}$	$(A/\lambda)^{1.37}$	$(2 \times Dh \times Re)/\lambda)^{0.897}$	f_{wavy}
100	0.0105	0.105	0.001232	0.5762	0.042658	2.149289464	0.6136588
200	0.0105	0.105	0.001232	0.2881	0.042658	4.002384573	0.3226236
300	0.0105	0.105	0.001232	0.1920667	0.042658	5.758013453	0.2248744
400	0.0105	0.105	0.001232	0.14405	0.042658	7.453199085	0.1756297
500	0.0105	0.105	0.001232	0.11524	0.042658	9.104812439	0.1458569
600	0.0105	0.105	0.001232	0.0960333	0.042658	10.722513	0.1258553
700	0.0105	0.105	0.001232	0.0823143	0.042658	12.31254559	0.1114576
800	0.0105	0.105	0.001232	0.072025	0.042658	13.87927012	0.1005751
900	0.0105	0.105	0.001232	0.0640222	0.042658	15.42589748	0.0920448

Table 13 shows the estimation process of the friction factor with upgraded hydraulic diameters for Reynolds numbers ranging from 100 to 900. It is visible that f_{wavy} is higher than the values of $f_{Straight}$ in all values of Reynolds numbers, which is unfamiliar in Table 10.

Table 14: New operating length estimation for the current single channel wavy geometry.

Re	ρ (Kg/m3)	D_h (m)	μ(kg/ms)	U_{avg} (m/s)	U^2avg (m^2/s^2)	f_{wavy}	ΔP_{cap} (Pa)	L_{max} (mm)
100				0.03269	0.00107	0.613659		733.83842
200				0.06538	0.00427	0.322624		348.95647
300				0.09807	0.00962	0.224874		222.50756
400				0.13076	0.01710	0.17563		160.25423
500	784.6	0.001232	0.000316	0.16345	0.02672	0.145857	153.2467	123.49811
600				0.19615	0.03847	0.125855		99.392413
700				0.22884	0.05237	0.111458		82.4559
800				0.26153	0.06840	0.100575		69.961165
900				0.29422	0.08656	0.092045		60.400835

The friction factor (and hence the pressure drop) is greatly increased by the waviness; however, the effect decreases with higher Reynolds numbers because viscosity has less of an impact. Considering Table 14 and Table 7, $L_{max} \geq L_{1\lambda}$ to surround the half surface of the battery, which is the primary objective of this thesis work. For further calculation, the length of the channel (L_{ch}) has been considered 120 mm, where $L_{1\lambda} > L_{ch}$ (120mm) > $L_{max,}$ and can operate in all conditions below Re 500. As from Table 14, operating lengths from Re 600 to Re 900 are almost adjacent to 120 mm rather than the high variation from Re 100 to 500. So, it can be considered that a 120 mm heat pipe can be sustainable and capable of transmitting heating and cooling from Re 100 to Re 900. And can also surround 2 batteries ($L_{1\lambda}$ (114.60) >120mm). Even, there is a risk of the liquid drying out at Re 800 and Re 900.

Figure 18 illustrates the 2D and 3D geometry of 120 mm heat pipe merging with 2 batteries. Also, cross cross sectional view of the heat pipe is presented. The battery and heat pipe is arranged in such a way that each of the heat pipes covers two individual batteries, and each of the batteries covers two heat pipes. So all the battery's heat surface cylindrical area is certainly covered by the heat pipe, which will effectively increase the contact area with the heat pipe and so on, better thermal distribution.

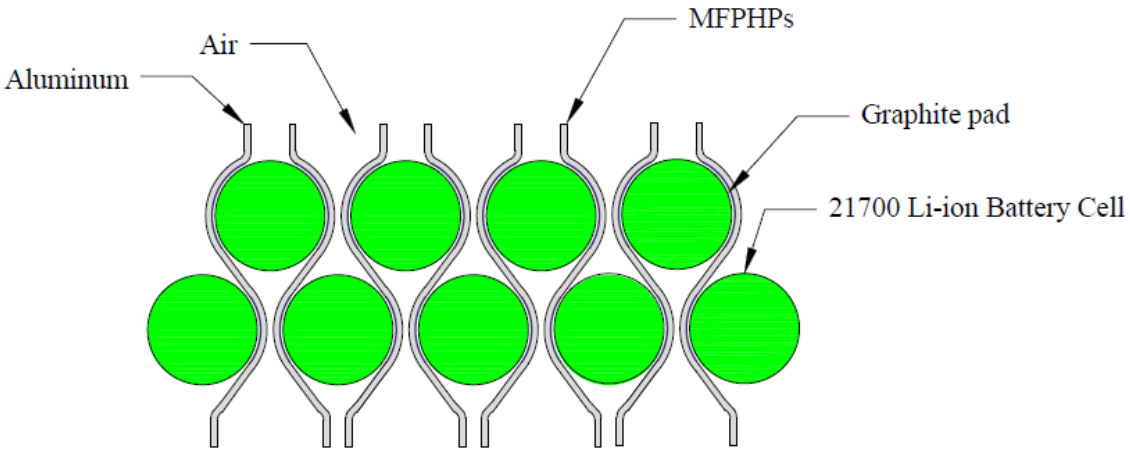

(a)

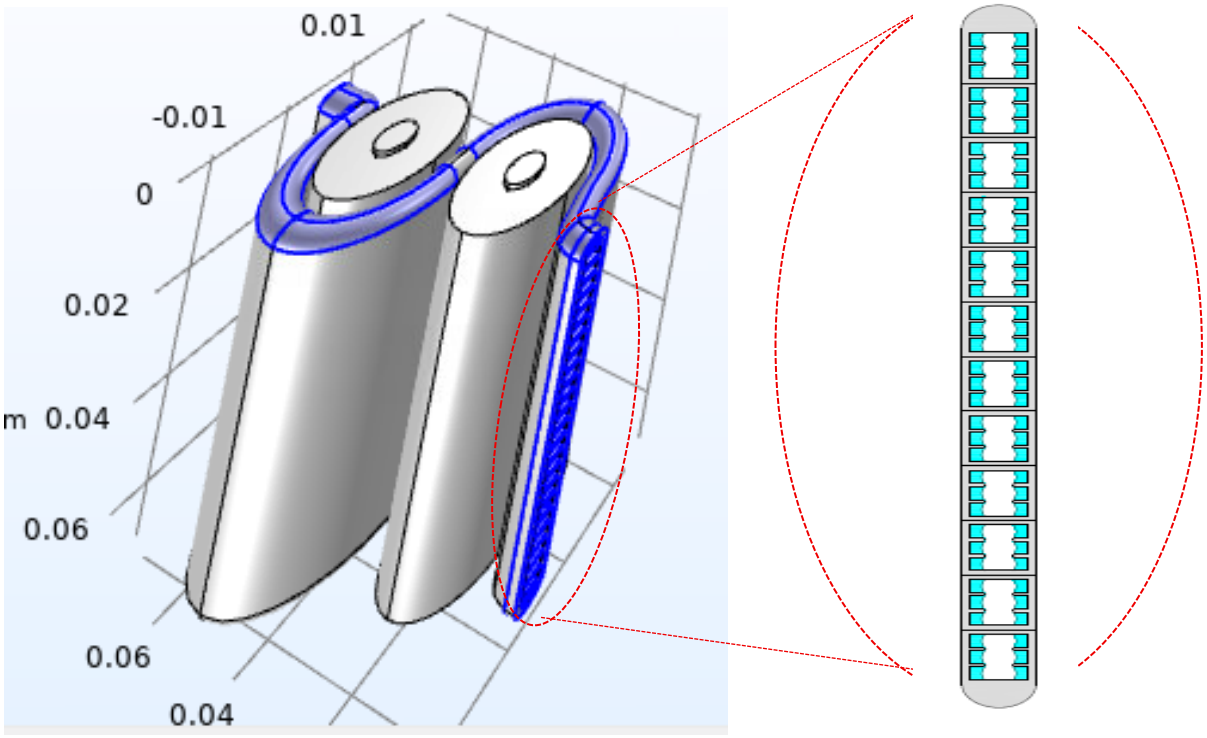

(b)

Figure 18: (a) sample model of proposed wavy grooved aluminum flat plate heat pipe (WFPHP) with battery arrangement; (b) 3D sample model of a single proposed wavy grooved aluminum flat plate heat pipe with individual acting heat pipes array (WFPHP).

4.4 Heat pipe integrated hybrid liquid based thermal management system

The proposed battery thermal management system (BTMS) as shown in Figure 19, which specifically considers 21700 format cylindrical lithium-ion cells, is made to control the intricate and fluctuating thermal requirements of the battery modules and the cabin of electric vehicles. Micro flat plate heat pipes (MFPHPs), which come into direct thermal contact with the battery cells, are a key component of the design. By facilitating quick and even heat flow across the battery pack, these passive two phase devices improve thermal reactivity and lessen temperature gradients between cells. A bidirectional heat exchanger system, which is connected to a refrigeration cycle based on vapor compression, is connected to the heat pipes via a fluid loop. By combining passive and active thermal management strategies, the system may achieve great thermal efficiency while using little energy and can be adjusted to various climatic circumstances.

With the addition of several electronically controlled expansion valves (EEVs), 3 way valves, flow control valves, and two evaporators and condensers, the system runs on a single loop heat pump cycle. These parts use three main operating modes to dynamically transport refrigerant according to thermal demands: simultaneous cabin heating and battery cooling, combination heating, and combined battery and cabin cooling. High pressure compressor refrigerant is partially subcooled in the internal condenser and condensed in the external heat exchanger when the battery and cabin cooling mode is engaged. It is then routed into two distinct evaporators after being enlarged using EEVs. The car cabin is cooled by one evaporator, while the bidirectional heat exchanger attached to the battery module through the MFPHPs is cooled by the other. The battery may stay within its acceptable operating range even in high ambient or heavy load situations thanks to the MFPHPs' effective ability to pull heat away from the battery cells and transmit it to the refrigerant loop for disposal.

When the system is in heating mode in Figure 19 (b), it works in reverse to provide thermal energy to the battery and the cabin. To warm the cabin, the compressor first circulates high temperature refrigerant through the internal condenser. The external heat exchanger then partially rejects the heat. The battery is subsequently warmed by some of this heat via the MFPHP network and the second bidirectional heat exchanger.

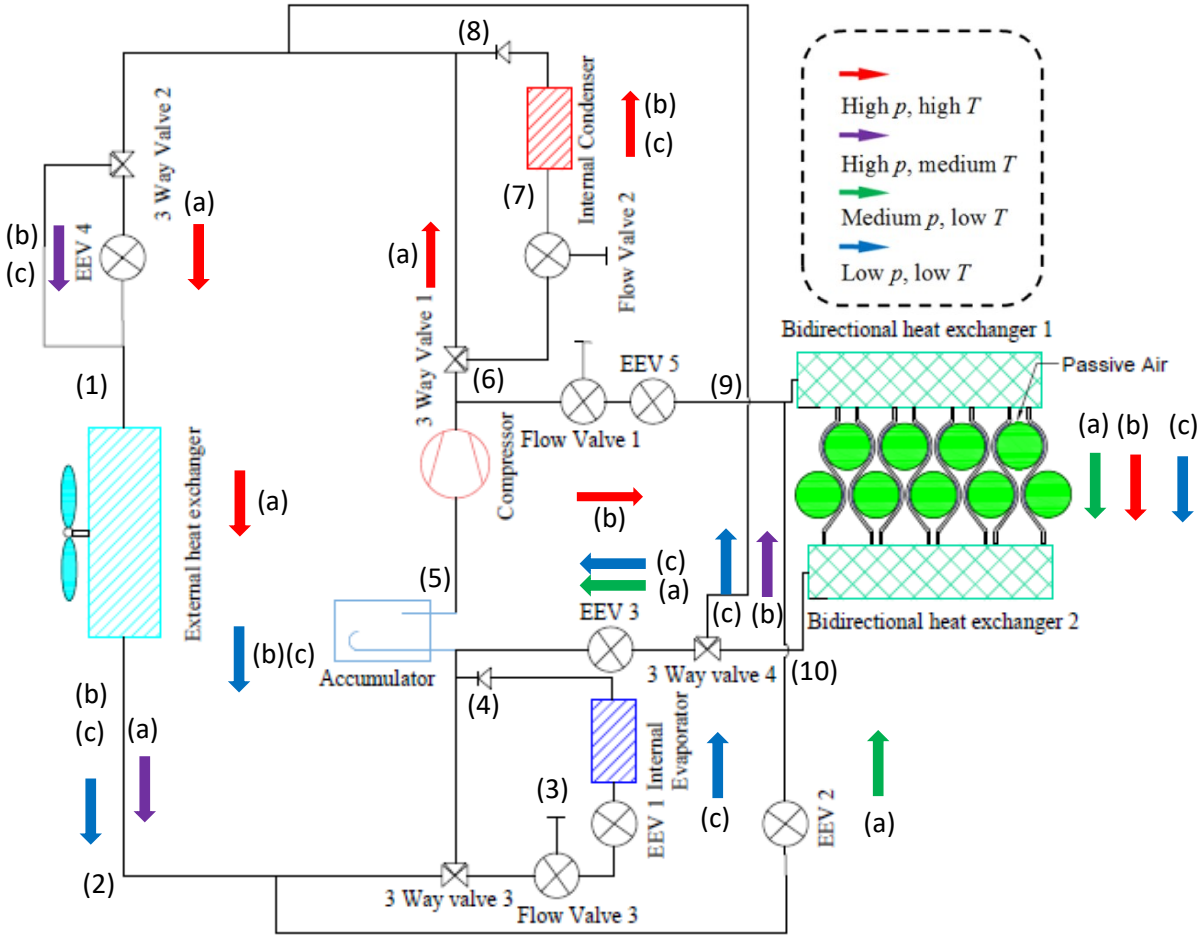

Figure 19: (a) schematic of the cabin and battery mix cooling mode with MFPHPs; (b) schematic of the cabin and battery mix heating mode with MFPHPs; (c) schematic of the cabin heating and battery cooling mode with MFPHPs.

By properly balancing thermal loads between the two domains, this parallel heating arrangement maximizes comfort and guarantees that the battery reaches the ideal temperature for effective operation or charging. The amount of heat given to each zone may be precisely managed thanks to real time expansion and valve position control based on temperature feedback.

As seen in Figure 19(c) operating mode, when the cabin has to be heated and the battery needs to be cooled, the system's ability to decouple cabin and battery temperature regulation is one of its most sophisticated features. In this mode, the refrigerant is split between a

condenser that heats the cabin circuit and an evaporator that cools the battery circuit. Careful flow control and the heat pipes' phase change capacity, which passively transfers heat away from the battery while heat is being supplied elsewhere, enable this dual direction management. This mode is particularly helpful during fast charging events in cold climes where passengers still need cabin heating but the battery may need cooling due to excessive internal heat generation.

To maximize thermal regulation for 21700 Li-ion batteries, a heat pipe integrated hybrid liquid based Battery Thermal Management System (BTMS) combines the accuracy of a refrigerant driven liquid loop with the passive efficiency of wavy flat plate heat pipes (FPHPs). This device uses phase change mechanisms to passively absorb heat from the battery surface using aluminum 6061 FPHPs with axial microgrooves (1.1 mm depth, 1.4 mm width) filled with acetone. Acetone's low viscosity and high latent heat (517 kJ/kg) allow for quick heat transfer to a bidirectional heat exchanger that is connected to a refrigerant circuit.

The effectiveness of the micro flat plate heat pipes can significantly contribute to improving the system's thermal efficiency in all operating modes. The flattened design of these MFPHPs allows for more surface contact with the battery cell housing, which facilitates effective heat dispersion and pickup. Rapid liquid return to the evaporation zone is facilitated by the internal capillary structures, which enable continuous functioning under a range of load and orientation conditions. To provide ideal thermal contact, the MFPHPs are clamped or fixed directly into the cylindrical cells' surfaces. By integrating these heat pipes, the system's thermal resistance can be greatly decreased, reducing the risk of thermal runaway and extending battery life.

The system comprises a series of electronically controlled expansion valves (EEV1 to EEV5) and 3 way valves (Valves 1 to 4) to flexibly change flow routes and manage refrigerant behavior under such a variety of settings. EEV1 and EEV2 control expansion into the evaporators during cabin and battery cooling, while EEV3 and EEV4 adjust refrigerant flow in the direction of the bidirectional heat exchangers. In order to control extra liquid refrigerant, avoid flooding, and maintain phase stability, accumulator tanks are positioned strategically. The EEVs control pressure drops and superheat situations for efficient phase control, while the 3 way valves reroute hot compressed refrigerant toward the internal and

external heat exchangers during heating modes. Real time distribution balance coordination between the cabin and battery modules is managed by flow valves 1 and 2.

To increase the effectiveness of heat transmission, the external and internal heat exchangers are built with a high fin density and optimal surface area. While the internal unit is tucked away close to the cabin HVAC system, the exterior unit usually interacts with the surrounding air or other cooling medium. Depending on the mode option and refrigerant flow direction, the bidirectional heat exchangers that directly interface with the MFPHPs can function as either condensers or evaporators. Because of its adaptability, the system can reverse heat flow pathways without requiring component replacement or mechanical disassembly. To improve total COP and lower parasitic losses, these exchangers are shielded from the environment to reduce thermal leakage.

This design's modular layout and small form factor are further advantages. The technology achieves great thermal density without appreciably adding weight or volume by integrating the bidirectional exchangers directly within the battery module casing and embedding the heat pipes within a thin thermal interface layer. For electric vehicle platforms, where mass and space are severely limited, its compactness is perfect. Additionally, the modular architecture improves maintainability and system longevity by allowing individual battery packs or cabin HVAC systems to be repaired or upgraded independently.

5 Performance Evaluation Parameters

Performance evaluation criteria, including the average Nusselt number, friction factors, and thermal resistance, are examined for the designed heat pipe in order to evaluate the thermal performance.

The first performance indicator is the average Nusselt number, which is given by (G. Xia et al. 2011)

$$Nu_{(avg)} = \frac{1}{L_{ch}} \int_{L_{ch}}^{0} Nu_x \, dx \qquad (15)$$

where L_{ch} is the length of the channel and Nu_x is the local Nusselt number that is defined as

$$Nu_{(x)} = \frac{h_x D_h}{k_f} \quad (16)$$

where k_f is the fluid thermal conductivity, and D_h is the channel hydraulic diameter

For the rectangular microchannel, three sided heating and cooling, Nusselt numbers in the thermally developing region are presented in G. Xia et al. 2011 as follows

$$Nu_{(x)} = 1.0958 \left[\frac{23.315+27038(x^*)+1783300\,(x^*)^2}{1+3049(x^*)+472520(x^*)^2-35714(x^*)^3}\right] \quad (17)$$

The dimensionless axial coordinate (x*) is defined as,

$$x^* = \frac{x}{D_h RePr} \quad (18)$$

The Prandtl number (Pr) for acetone as a working fluid can be calculated as

$$Pr = \frac{\mu\, Cp_f}{k_f} \quad (19)$$

From Table (9), using $\mu = 0.000316$ (kg/ms), $Cp_f = 2169$ (J/kgK) and $k_f = 0.153$ (W/mK)

So,

$$Pr = 4.479$$

Using Equations 16 to 19 with Re 300, Table 15 depicts how the local Nusselt number ($Nu_{(x)}$) and Local convective heat transfer coefficient (h_x) vary with the distance difference of 0.01m. In laminar flow, the thermal entrance effects are responsible for the initially high values of the convective coefficient h(x) and local Nusselt number $Nu_{(x)}$. The wall–fluid temperature differential is severe and the thermal boundary layer is very thin near the channel intake, resulting in high heat transfer coefficients. The wall gradient diminishes, the boundary layer deepens, and $Nu_{(x)}$ asymptotically approaches its fully developed value as the flow progresses downstream. In line with established correlations like Shah and London's (1978) for growing laminar convection, this behaviour is typical of thermally developing internal flows. Figure 20 illustrates the behaviour for Re 300 to Re 900.

Table 15: Estimation of Local Nusselt number along with local heat transfer coefficient

Re	D_h (m)	Pr	K	x (m)	x*	Nu (x)	h (x)
300	0.001232	4.4798	0.153	0	0	25.548577	3172.8346
				0.01	0.0060397	5.6605897	702.97908
				0.02	0.0120793	5.1089244	634.4687
				0.03	0.018119	4.8665972	604.37449
				0.04	0.0241587	4.7254186	586.84175
				0.05	0.0301983	4.6322251	575.26822
				0.06	0.036238	4.5660267	567.04714
				0.07	0.0422777	4.5166434	560.91432
				0.08	0.0483173	4.4784844	556.17542
				0.09	0.054357	4.4482065	552.41525
				0.1	0.0603966	4.4236814	549.36953
				0.11	0.0664363	4.4034876	546.86168
				0.12	0.072476	4.3866378	544.76915

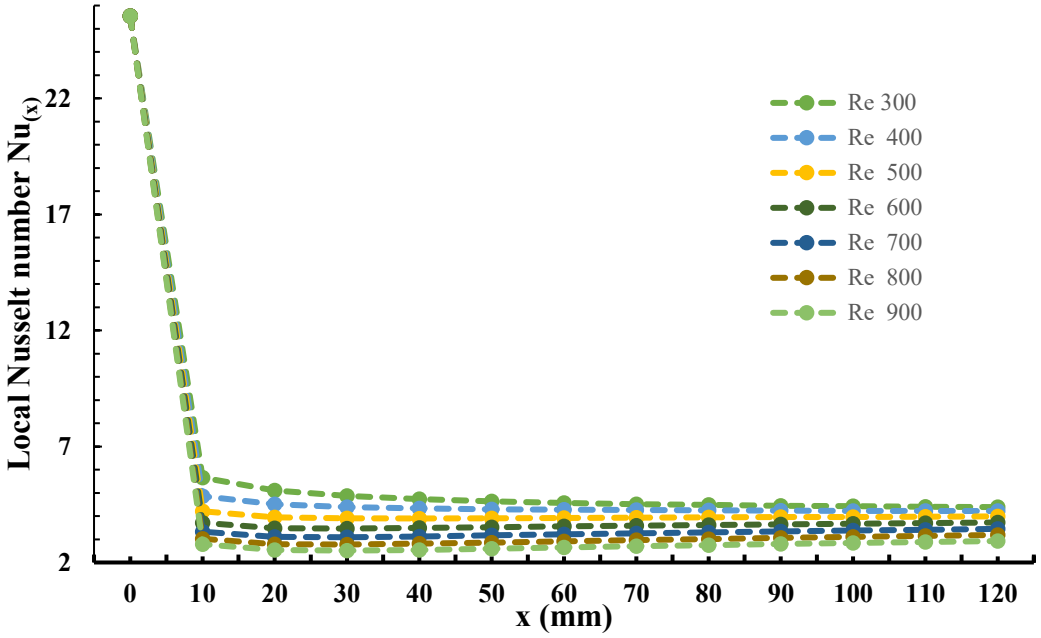

Figure 20: Variation of Local Nusselt numbers with distances and Reynolds numbers.

The average Nusselt number from Equation (15), can also be described as

$$\mathrm{Nu}_{(avg)} = \frac{1}{\mathrm{L_{ch}}} \int_{\mathrm{L_{ch}}}^{0} \mathrm{Nu_x}\, dx$$

$$\approx \frac{1}{L} \sum_i \frac{Nu_i + Nu_{i+1}}{2} \Delta x$$

Here, L=120 mm=0.12 m, and Δx=10 mm=0.01 m.

Table 16: Estimation of a single channel's Average Nusselt number and average heat transfer coefficient.

Re	$Nu_{(avg)} = Nu_{Straight}$	$h_{(avg)} = h_{Straight}$
300	5.572308	696.5385
400	5.236336	654.542
500	4.870508	608.8135
600	4.518529	564.816125
700	4.198146	524.76825
800	3.914386	489.29825
900	3.666375	458.296875

Table 16 and Figure 21 show how the average Nusselt number (Nu_{avg}) varies. along with the matching average convective heat transfer coefficient for a similar diameter of straight pipe,h_{avg} from 300 to 900 Reynolds numbers for the straight single channel. With an increase in Reynolds number, both parameters gradually decline from Nu_{avg} = 5.57 and h_{avg} = 696.5. Thermally growing laminar flows under conditions of constant wall heat flux exhibit this inverse pattern. The fluid residence time in the channel shortens with increasing flow rate, reducing the amount of time available for heat diffusion into the core region. This leads to a thicker thermal boundary layer and, ultimately, a lower mean temperature gradient at the wall.(Shah and London (1978))

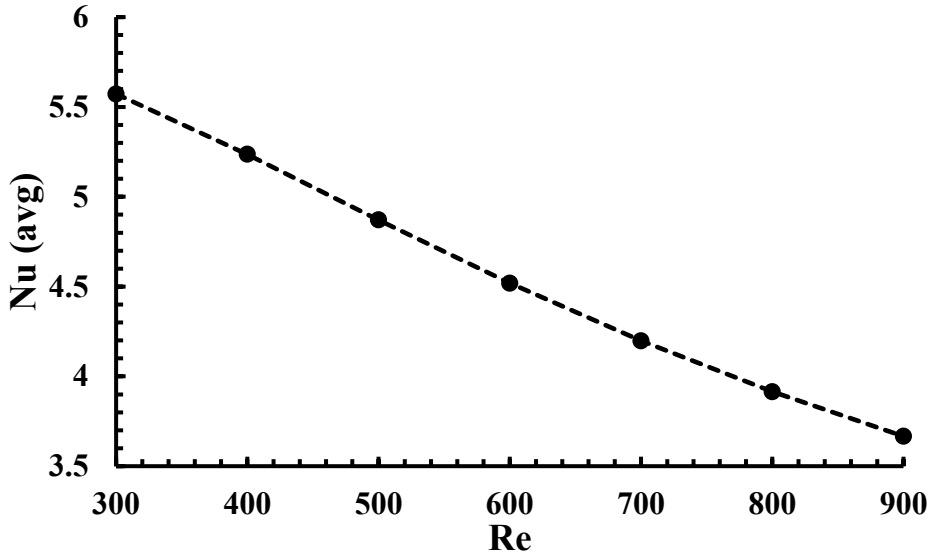

Figure 21: Variation of a single straight channel's average Nusselt number with Reynold's numbers.

(Sui et al. 2010) & (Rosaguti et al. 2006) two parameters of the Nusselt number enhancement and friction factor enhancement are expressed as follows (Equation 20 and Equation 21) to assess the increase of the Nusselt number and friction factor of the wavy patterns in comparison to the straight pattern.

$$E_{Nu} = \frac{Nu_{Wavy}}{Nu_{Straight}} \qquad (20)$$

$$E_f = \frac{f_{Wavy}}{f_{Straight}} \qquad (21)$$

According to (Ghorbani et. al 2022) to study both the thermal and hydraulic performance concurrently, the performance evaluation criteria (PEC) is delineated by Equation (22)

$$PEC_{wavy/straight} = \frac{{}^{Nu_{Wavy}}/_{Nu_{Straight}}}{\left({}^{f_{Wavy}}/_{f_{Straight}}\right)^{1/3}} \quad (22)$$

According to (Ghorbani et. al 2022), in Figure 22 for (A/λ) = 0.1 (case 3) $PEC_{wavy/straight}$ reaches from 2.25 at Re 300 to 3.0 at Re 900. Using this data, the Nusselt number for a similar geometry, wavy shape and average heat transfer coefficient has been estimated in Table 17. The variation of the average Nusselt number and heat transfer coefficient for straight and wavy structures has been shown in Figures 23 and 24.

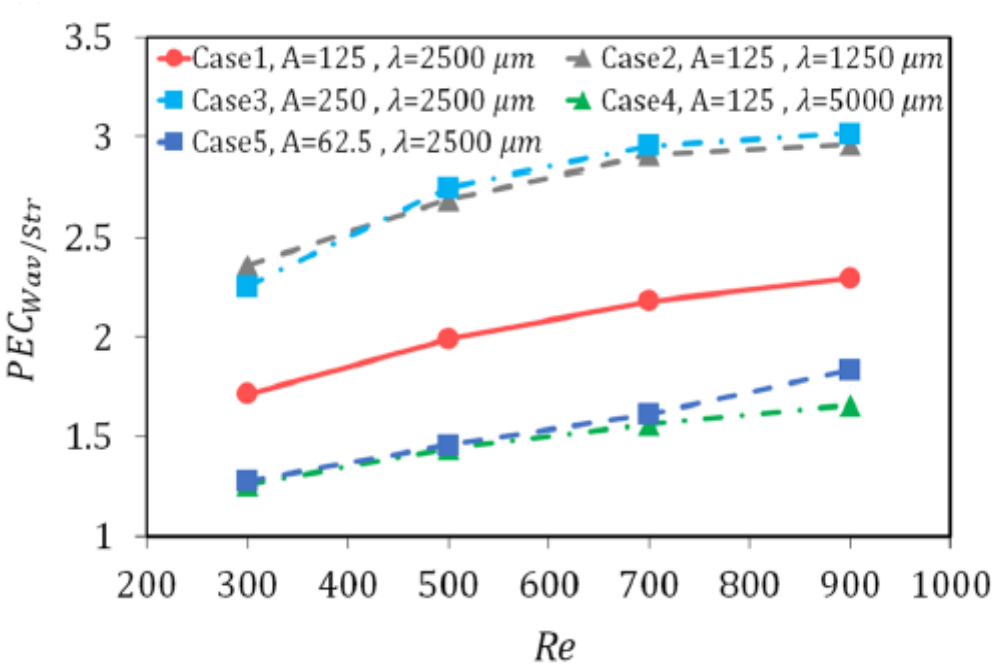

Figure 22: Performance evaluation criterion in relation to Reynolds number, with the straight pattern serving as the reference. (Ghorbani et. al 2022)

Table 17: estimation of average heat transfer coefficient and Nusselt number of the designed single wavy channel in relation to Reynolds number, with the straight pattern serving as the reference.

Re	$E_f = (f_{Wavy}/f_{Straight})$	**PEC** (Wavy/Straight)	$E_{Nu} = (Nu_{Wavy}/Nu_{Straight})$	$Nu_{avg(Straight)}$	$Nu_{avg(Wavy)}$	$h_{avg,Wavy}$
300	1.170814543	2.25	2.371438616	5.572308	13.214386	1651.798
400	1.219227206	2.5	2.670760167	5.236336	13.984998	1748.125
500	1.265679762	2.75	2.974682641	4.870508	14.488216	1811.027
600	1.310538091	2.8	3.064135131	4.518529	13.845383	1730.673
700	1.354048935	2.85	3.152992807	4.198146	13.236724	1654.591
800	1.396391234	2.9	3.241408021	3.914386	12.688122	1586.015
900	1.437701363	3	3.385926161	3.666375	12.414075	1551.759

For further calculations, the heat transfer coefficient of a wavy single channel has been considered 1676.284 W/m^2k. Which is the average value of all the corresponding average heat transfer coefficients for Re 300 to Re 900.

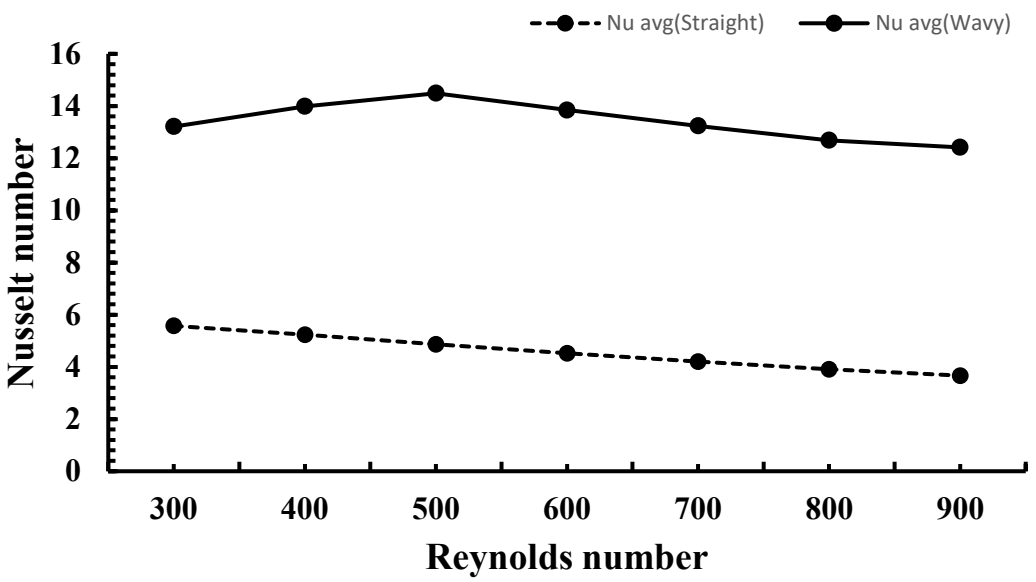

Figure 23: Average Nusselt numbers versus Reynolds number for straight and wavy shapes of similar geometry.

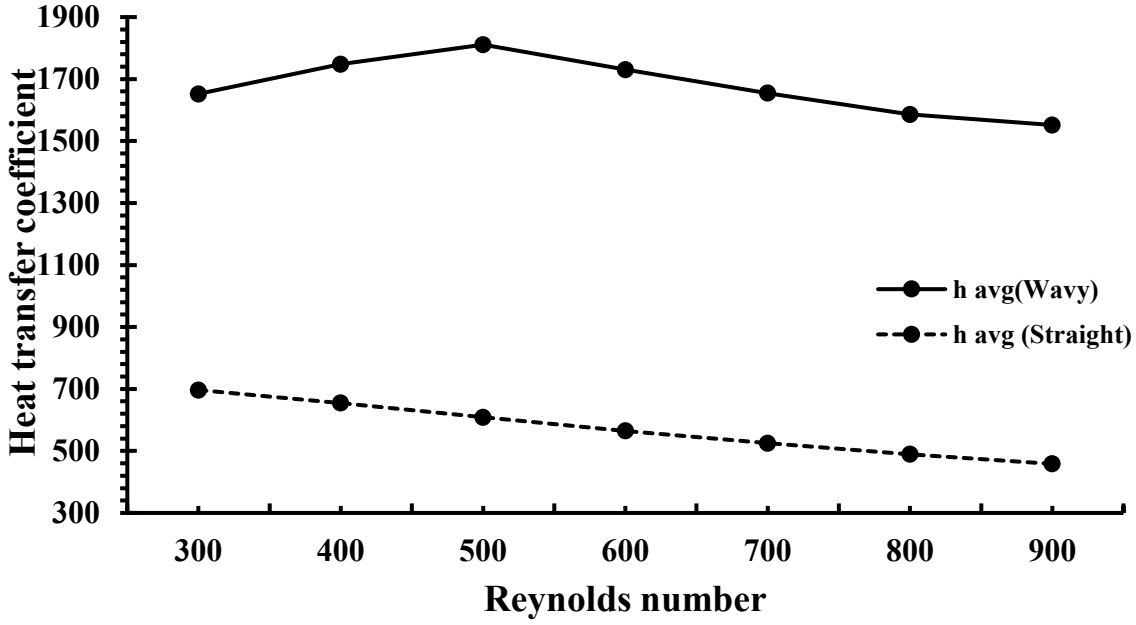

Figure 24: Average heat transfer coefficient versus Reynolds number for straight and wavy shapes of similar geometry.

5.1 Thermal Resistance Network:

The total thermal resistance of an individual identical heat pipe can be expressed by the laws of heat and mass transfer (L.M. Poplaski et al. 2016).

$$R_{th} = R_{th,contact} + R_{th,cond} + R_{th,vapor} + R_{th,conv} \quad (23)$$

$R_{th,contact}$ is thermal contact resistance (battery to heat pipe), $R_{th,cond}$ is the conduction resistance of heat pipe's metal wall, $R_{th,vapor}$ is vapor side (evaporation/condensation) resistance (estimate for phase change limited condensate/evaporation; strongly depending on geometry; order of magnitude) and $R_{th,conv}$ is the convective thermal resistance.

In this study, only convective thermal resistance is considered. The other components, like contact resistance ($R_{th,contact}$), conductive resistance ($R_{th,cond}$) through the wavy heat pipe wall and vapor phase resistance ($R_{th,vapor}$) are ignored due to their relatively small magnitudes and the significant increase in modeling complexity associated with their inclusion. Such as, One dimensional conduction formula $R_{th,cond} = \frac{t}{k_{Al}\, A_{contact}}$ is only accurate if heat moves through the thickness all the way with the same cross sectional area. A circular (or partially wrapped) battery meeting a plate causes heat to disperse laterally within the plate, increasing the real conduction resistance. Resistance that spreads (constriction) must be included. (Incropera et al. 2011). Accounting for such multidimensional effects would require complex analytical or numerical modelling with detailed geometric and material characterization. Similarly, the contact interface employs a high conductivity medium that minimizes interfacial losses, while the vapor phase region inside the heat pipe possesses an inherently high effective thermal conductivity due to phase change-driven vapor transport (L.M. Poplaski et al. 2016). As these resistances are comparatively small and their detailed inclusion would substantially increase computational complexity, the analysis in this work focuses on the dominant convective resistance ($R_{th,conv}$), which governs the overall thermal performance of the system (L.M. Poplaski et al. 2016).

According to the laws of convection heat transfer, the convective thermal resistance for heat pipe can be expressed as,

$$R_{th,conv} = \frac{1}{h \times A_{W,n}} \quad (24)$$

Now, $P = 2(W_{ch,new} + H_{ch,new}) = 2\ (0.0014 + 0.0011) = 0.005$ m = 5 mm.

Wetted area of each channel,

$A_{ch,new} = P \times L_{ch} = 0.005$ m $\times$ 0.12 m = 0.0006 m^2 = 600 mm^2.

Total wetted area for 3 channels on each side,

$A_{W,n1} = 3 \times A_{ch,new} = 3 \times 0.0006\ m^2 = 0.0018\ m^2 = 1800\ mm^2$.

Wetted area of channels on each acting individual heat pipe,

$A_{W,n} = 2 \times A_{W,n1} = 2 \times 0.0018\ m^2 = 0.0036\ m^2 = 3600\ mm^2$.

Here, h is the heat transfer coefficient and $A_{W,n}$ is the wetted area of an individual heat pipe. So, from Equation (24), using the average heat transfer coefficient from Table 17

$$R_{th,conv} = \frac{1}{1676.284\frac{W}{m^2k} \times 0.0036\ m^2}$$

$$= 0.1657\ k/W$$

According to Table 12, there are 12 identical heat pipes side by side, all connected to the same heat source area (e.g., a battery module) and transferring heat to the same condenser and evaporator region.

So, for n identical parallel heat flow pathways, so, according to Incropera et al. 2011, the total convective thermal resistance of 12 parallelly connected total heat pipes is

$$\frac{1}{R_{total,conv}} = 12 \times \frac{1}{R_{th,conv}}$$

$$R_{total,conv} = \frac{0.1657\ k/W}{12}$$

$$= 0.01381\ k/W$$

So, from the entire analysis, a 120 cm wavy aluminium heat pipe with 12 individual identical parallelly connected heat pipes under it, with a Hydraulic diameter of 0.001232 m (single channel width 1.4mm and height 1.1mm), and three channels on each side of the heat pipe can provide a total conductive thermal resistance of 0.01381 k/W.

6 Conclusions

The goal of this thesis was to design and develop a flexible wavy flat plate heat pipe (WFPHP) based system that incorporates with the existing HVAC system in EVs. The responsiveness to changing thermal loads and inability to enable proper thermal control are the main drawbacks of traditional passive heat pipes that the technology was designed to explicitly solve. The work successfully demonstrated through conceptual design and analytical analysis that a thermally responsive and orientation independent solution can be created by combining WFPHPs. Through analytical analysis based on heat pipe design with numerical analysis, it has been shown that this integrated system can maintain strict temperature control and homogeneity, thereby achieving the work objectives.

The design and analysis of an active two phase BTMS that transfers heat via acetone boiling/condensation constitutes the primary contribution. Theoretically, the thesis also demonstrates that the suggested system achieves its objectives by providing better temperature regulation by surrounding each of the batteries than previous designs and enabling both controlled heating and effective cooling.

Direct liquid/refrigerant loops, passive capillary heat pipes, and loop heat pipes (LHPs) are examples of conventional heat pipe based BTMS techniques. The suggested WFPHP, on the other hand, incorporates valves to permit dynamic mode switching and to deliver a steady flow independent of orientation. EVs typically have traditional liquid cooled systems, such as water/glycol coolant or refrigerants like R1234yf, which provide good cooling power and integrated thermal routing (Tesla's Octovalve, for instance, uses valve networks in a single coolant loop). Similar to valve controlled routing, the proposed system takes advantage of the latent heat of phase shift rather than just sensible heat in the fluid. In a nutshell, the WFPHP combines the best features of both systems: it adds the accuracy and orientation independence of liquid loop while maintaining the high conductivity and reversible flow of heat pipes. Compared to cold plate designs or completely passive heat pipes, this hybrid technique numerically showed that it should perform well.

The performance and safety of EV batteries depend on efficient heat regulation. Li-ion cells produce heat as they charge or discharge, and if this heat is not sufficiently removed, it can rise quickly, hastening aging or possibly causing thermal runaway. Battery longevity and efficiency can be improved by the suggested WFPHP, which keeps cells within their ideal temperature range. According to industry experts, thermal management solutions guarantee that batteries run at the ideal temperatures for maximum performance and range. Electric vehicles benefit greatly from the dual cooling/heating capacity since it can preheat batteries in cold climates without the need for resistive heaters alone and avoid overheating under heavy loads. Improved thermal uniformity and ideal temperature control can prolong cycle life, lowering the need for battery replacements and so saving resources from a sustainability standpoint. Moreover, these acetone based heat pipes use an organic fluid with a comparatively low global warming potential and do not require a high power compressor. The environmental benefits of passive heat pipe systems are significant when considering life cycle impact. For instance, (Monticelli et al. 2025) conducted a life cycle assessment (LCA) comparing a passive loop heat pipe BTMS and an active cold plate BTMS. They discovered that, in comparison to the cold plate, the LHP system lowered system weight by around 40% and greenhouse gas emissions by approximately 52%. These findings imply that using heat pipe technology can result in significant reductions in energy use and emissions, even if our system is active and uses pump power. All things considered, the suggested WFPHP has obvious industrial significance for EVs of the future and may help achieve the more general objectives of energy efficiency and less environmental impact.

Only conceptual design has been done at this time. There has not yet been experimental validation. Fluid leakage, liquid drying, inadequate valve sealing, and environmental heat losses are examples of unmodeled effects that may be discovered during real hardware testing. Another issue is the compatibility of materials. Despite being flammable and volatile, acetone works well as a working fluid; therefore, it will be important to make sure it is chemically compatible with the metals and membranes in the loop. Comparatively speaking to passive designs, the additional parts (pump, EEV, and valves) raise system complexity, possible failure sites, and expense. Some losses (such as pressure drop in long tubing) were overlooked in the simulation, which assumed perfect flow control. Additionally, this study concentrated on the 21700 cell model; scaling to entire battery modules or packs will present additional difficulties due to packaging limitations, uneven

flow distribution, and connection with the cooling infrastructure that is already in place. These restrictions advise prudence: although the results show promise as a theoretical proof of concept, actual performance has to be verified.

Experimental prototyping is the next step to further this research. It would be possible to monitor actual thermal performance and assess control measures by constructing a lab scale WFPHP module centered around a 21700 cell. The dependability of the pump, valves, and wick under repeated heat loads should be evaluated using long term cycle testing. In order to automatically modulate pump speed and EEV position based on cell temperatures, integration with a battery management system (BMS) is advised. Safety could be increased by investigating alternate working fluids and wick materials (such as water or ethanol with corrosion inhibitors, or more recent low GWP refrigerants). To build multi cell headers and guarantee uniform cooling over an array of cells, pack level studies are also required. The picture would be completed by a thorough examination of control algorithms and energy consumption (pump/EEV power) in relation to cooling benefits. A life cycle or cost benefit analysis akin to earlier research may be included in such work.

By introducing a flexible WFPHP based system that functions dependably in a variety of scenarios, this study advances the field of battery heat management. By providing fluid control, bidirectional heat transfer, and orientation independent operation, it fills important gaps in existing heat pipe technology. The findings provide a strong basis for further experimental verification and advancement toward practical implementation in energy storage and next generation electric car applications.

References

Afzal, A. et al. (2023) 'A critical review on renewable battery thermal management system using heat pipes', Journal of Thermal Analysis and Calorimetry. Available at: https://doi.org/10.1007/s10973-023-12100-9.

Ahn, J.H. et al. (2014) 'Heating performance characteristics of a dual source heat pump using air and waste heat in electric vehicles', Applied Energy, 119, pp. 1–9. Available at: https://doi.org/10.1016/j.apenergy.2013.12.065.

Al Jubori, A.M. and Jawad, Q.A. (2022) 'Experimental thermal performance assessment of aluminum and copper heat pipes for refrigerated container applications', International Journal of Refrigeration, 133, pp. 90–98. Available at: https://doi.org/10.1016/j.ijrefrig.2021.09.029.

AMS Battery (2021) Product Specifications Li Ion 21700 5000mAh 18Wh. Available at: https://www.ams-battery.com/wp-content/uploads/2021/06/lithium-ion-21700.pdf (Accessed: 22 May 2025).

ASHRAE (2022) ASHRAE Refrigerant Designations. Available at: https://www.ashrae.org/technical-resources/standards-and-guidelines/ashrae-refrigerant-designations (Accessed: 18 June 2025).

batterybuddy.eu (2024) *18650 vs 21700 Batteries: In-Depth Comparison and Analysis*. Available at: https://batterybuddy.eu/battery-types-and-selection/18650-vs-21700-batteries-in-depth-comparison-and-analysis (Accessed: 21 May 2025).

Bernagozzi, M. et al. (2021) 'Novel battery thermal management system for electric vehicles with a loop heat pipe and graphite sheet inserts', Applied Thermal Engineering, 194. Available at: https://doi.org/10.1016/j.applthermaleng.2021.117061.

Bernagozzi, M., Georgoulas, A. et al. (2023) 'Heat pipes in battery thermal management systems for electric vehicles: A critical review', Applied Thermal Engineering. Elsevier Ltd. Available at: https://doi.org/10.1016/j.applthermaleng.2022.119495.

Boonma, K. et al. (2022) 'A Review of the Parameters Affecting a Heat Pipe Thermal Management System for Lithium-Ion Batteries', Energies. MDPI. Available at: https://doi.org/10.3390/en15228534.

Butler, D., Ku, J. and Swanson, T. (2001) Advances in Capillary Pumped Loop Technology for Spacecraft Thermal Control. NASA Technical Memorandum. Available at: https://ntrs.nasa.gov/api/citations/20020013939/downloads/20020013939.pdf (Accessed: 29 June 2025).

Cao, W. et al. (2019) 'Thermal modeling of full-size-scale cylindrical battery pack cooled by channeled liquid flow', International Journal of Heat and Mass Transfer, 138, pp. 1178–1187. Available at: https://doi.org/10.1016/j.ijheatmasstransfer.2019.04.137.

Chen, G. et al. (2020) 'Thermal performance enhancement of micro-grooved aluminum flat plate heat pipes applied in solar collectors', Renewable Energy, 146, pp. 2234–2242. Available at: https://doi.org/10.1016/j.renene.2019.08.083.

Duan, L. et al. (2022) 'Research on the Manufacturing Process and Heat Transfer Performance of Ultra-Thin Heat Pipes: A Review', Materials, 15(15), p. 5459. Available at: https://doi.org/10.3390/ma15155459.

Dunn, P.D. and Reay, D.A. (2014) Heat Pipes. 6th ed. Oxford: Elsevier.

Engineering ToolBox (2022) Acetone - Thermophysical Properties. Available at: https://www.engineeringtoolbox.com/acetone-2-propanone-dimethyl-ketone-properties-d_2036.html (Accessed: 27 June 2025).

Faghri, A. (1995) Heat Pipe Science and Technology. Taylor & Francis.

Faghri, A. and Khrustalev, D. (1996) Miniature Flat Heat Pipes with Axial Microgrooves. NASA Technical Report. Available at: https://ntrs.nasa.gov/api/citations/19970000389/downloads/19970000389.pdf (Accessed: 14 September 2025).

Gao, Y. et al. (2019) 'A physics-based model for battery failure in phosphate-based lithium ion batteries', Reliability Engineering & System Safety, 190, 106499. Available at: https://doi.org/10.1016/j.ress.2019.106499.

Garud, K.S. et al. (2023) 'A Review of Advanced Cooling Strategies for Battery Thermal Management Systems in Electric Vehicles', Symmetry. Multidisciplinary Digital Publishing Institute (MDPI). Available at: https://doi.org/10.3390/sym15071322.

Ghorbani, N. et al. (2022) 'Investigation of wavy microchannel ability on electronic devices cooling with the case study of choosing the most efficient microchannel pattern', Scientific Reports, 12, 5882. Available at: https://doi.org/10.1038/s41598-022-09859-6.

Guo, J. and Jiang, F. (2021) 'A novel electric vehicle thermal management system based on cooling and heating of batteries by refrigerant', Applied Thermal Engineering, 181, p. 115913. Available at: https://doi.org/10.1016/j.enconman.2021.114145.

He, L. et al. (2023) 'Review of thermal management system for battery electric vehicle', Journal of Energy Storage. Elsevier Ltd. Available at: https://doi.org/10.1016/j.est.2022.106443.

Hu, X. et al. (2020) 'Battery warm-up methodologies at subzero temperatures for automotive applications: Recent advances and perspectives', Progress in Energy and Combustion Science. Elsevier Ltd. Available at: https://doi.org/10.1016/j.pecs.2019.100806.

Huang, G. et al. (2018) 'Thermal characterisation of micro flat aluminium heat pipe arrays by varying working fluid and inclination angle', Applied Sciences (Switzerland), 8(7). Available at: https://doi.org/10.3390/app8071052.

Huber, M.L. (2016) Thermal Conductivity of Liquids as a Function of Temperature. NIST Technical Reference Data, Thermophysical Properties Division. Available at: https://tsapps.nist.gov/publication/get_pdf.cfm?pub_id=931484 (Accessed: 13 September 2025).

Incropera, F.P. et al. (2011) Fundamentals of Heat and Mass Transfer. 7th ed. Hoboken, NJ: John Wiley & Sons.

Kang, Y. et al. (2024) 'Application of Refrigerant Cooling in a Battery Thermal Management System under High Temperature Conditions: A Review', ACS Omega. American Chemical Society, pp. 25591–25609. Available at: https://doi.org/10.1021/acsomega.4c02902.

Khoshvaght-Aliabadi, M., Hassani, S. and Mazloumi, S.H. (2017) 'Thermal and hydraulic characteristics of a nanofluid flow in a rib–groove channel', Experimental Thermal and Fluid Science, 89, pp. 89–107. Available at: https://doi.org/10.1016/j.expthermflusci.2017.08.017.

Kumar, R., Dwivedi, A. and Goel, V. (2024) 'A Review on Heat Pipe-Assisted Thermal Management Systems in Electrical Vehicles for Lithium-Ion Batteries', in Singh, K.M. et al. (eds) Fluid Mechanics and Fluid Power, Volume 1. Lecture Notes in Mechanical Engineering. Springer, Singapore. Available at: https://doi.org/10.1007/978-981-99-7827-4_15.

Li, W. et al. (2023) 'A Review on Battery Thermal Management for New Energy Vehicles', Energies, 16(13), p. 4845. Available at: https://doi.org/10.3390/EN16134845.

Li, X. et al. (2023) 'Machine learning approach to predict CO2 solubility in potassium and sodium-based amino acid salt solutions', ACS Omega, 8(3), pp. 3018–3027. Available at: https://doi.org/10.1021/acsomega.2c05381.

Lin, C. et al. (2021) 'Heat generation quantification of high-specific-energy 21700 battery cell using average and variable specific heat capacities', Applied Thermal Engineering, 184. Available at: https://doi.org/10.1016/j.applthermaleng.2020.116215.

Lin, K.T. and Wong, S.C. (2013) 'Performance degradation of flattened heat pipes', in Applied Thermal Engineering, pp. 46–54. Available at: https://doi.org/10.1016/j.applthermaleng.2012.06.001.

Linstrom, P.J. and Mallard, W.G. (eds.) (2023) NIST Chemistry WebBook, NIST Standard Reference Database Number 69. National Institute of Standards and Technology, Gaithersburg MD. Available at: https://webbook.nist.gov/cgi/cbook.cgi?ID=C67641 (Accessed: 13 September 2025).

Liu, H. et al. (2017) 'Thermal issues about Li-ion batteries and recent progress in battery thermal management systems: A review', Energy Conversion and Management. Elsevier Ltd, pp. 304–330. Available at: https://doi.org/10.1016/j.enconman.2017.08.016.

Maiorino, A. et al. (2024) 'A review on thermal management of battery packs for electric vehicles', Applied Thermal Engineering. Elsevier Ltd. Available at: https://doi.org/10.1016/j.applthermaleng.2023.122035.

MatWeb (2023) *Aluminum 6061-T6 Material Properties*. Available at: https://asm.matweb.com/search/specificmaterial.asp?bassnum=ma6061t6 (Accessed: 13 September 2025).

Monticelli, M. et al. (2025) 'A Comparative Life Cycle Analysis of an Active and a Passive Battery Thermal Management System for an Electric Vehicle: A Cold Plate and a Loop Heat Pipe', World Electric Vehicle Journal, 16(2). Available at: https://doi.org/10.3390/wevj16020100.

NIST Chemistry WebBook (2023) *Acetone (CAS Number: 67-64-1)*. National Institute of Standards and Technology. Available at: https://webbook.nist.gov/cgi/fluid.cgi?ID=C67641&Action=Page (Accessed: 14 September 2023).

OpenInverter Community (2019) Tesla Model S/X A/C Compressor. Available at: https://openinverter.org/wiki/Tesla_Model_S/X_A/C_Compressor (Accessed: 27 June 2025).

Poplaski, L.M., Faghri, A. and Bergman, T.L. (2016) 'Analysis of internal and external thermal resistances of heat pipes including fins using a three-dimensional numerical simulation', International Journal of Heat and Mass Transfer, 102, pp. 455–469. Available at: https://doi.org/10.1016/j.ijheatmasstransfer.2016.05.116.

Radian Thermal Products Inc. (2025) Liquid Cooling Cold Plate Performance. Available at: https://radianheatsinks.com/wp-content/uploads/2025/03/Liquid-Cooling-Cold-Plate-Performance.pdf (Accessed: 30 June 2025).

REDWAY POWER (2025) How Many 21700 Batteries Does a Tesla Have? Available at: https://www.redwaybattery.com/how-many-21700-batteries-does-a-tesla-have/ (Accessed: 19 June 2025).

Reay, D.A. and Kew, P.A. (2006) Heat Pipes: Theory, Design and Applications. 5th ed. Oxford: Butterworth-Heinemann.

Rosaguti, N.R., Fletcher, D.F. and Haynes, B.S. (2006) 'Laminar flow and heat transfer in a periodic serpentine channel with semi-circular cross-section', International Journal of Heat and Mass Transfer, 49(17-18), pp. 2912–2923. Available at: https://doi.org/10.1016/j.ijheatmasstransfer.2006.02.015.

Sato, N. (2001) 'Thermal behavior analysis of lithium-ion batteries for electric and hybrid vehicles', Journal of Power Sources, 99(1–2), pp. 70–77. Available at: https://doi.org/10.1016/S0378-7753(01)00478-5.

Shah, R.K. and London, A.L. (1978) Laminar Flow Forced Convection in Ducts. New York: Academic Press.

Shahjalal, M. et al. (2021) 'A review of thermal management for Li-ion batteries: Prospects, challenges, and issues', Journal of Energy Storage. Elsevier Ltd. Available at: https://doi.org/10.1016/j.est.2021.102518.

Shaeri, M.R., Attinger, D. and Bonner, R.W. (2018) 'Vapor chambers with hydrophobic and biphilic evaporators in moderate to high heat flux applications', Applied Thermal Engineering, 130, pp. 83–92. Available at: https://doi.org/10.1016/j.applthermaleng.2017.11.051.

Sui, Y., Teo, C.J. and Lee, P.S. (2010) 'Fluid flow and heat transfer in wavy microchannels', International Journal of Heat and Mass Transfer, 53(13–14), pp. 2760–2772. Available at: https://doi.org/10.1016/j.ijheatmasstransfer.2010.02.022.

Sui, Y., Lee, P. and Teo, C. (2011) 'An experimental study of flow friction and heat transfer in wavy microchannels with rectangular cross section', International Journal of Thermal Sciences, 50(12), pp. 2473–2482. Available at: https://doi.org/10.1016/j.ijthermalsci.2011.06.017.

Tang, H. et al. (2024) 'A review of fabrication and performance of heat pipes with grooved wick structure', Applied Thermal Engineering. Elsevier Ltd. Available at: https://doi.org/10.1016/j.applthermaleng.2024.123949.

TechSteel (2023) Properties of 6061 Aluminum. Available at: https://www.techsteel.net/alloy/aluminum/6061 (Accessed: 13 September 2025).

Vapcell (2017) *18650 / 21700 Battery Internal Resistance Cold Testing*. Available at: https://budgetlightforum.com/t/18650-21700-battery-internal-resistance-cold-testing/55111 (Accessed: 29 June 2025).

Wang, G. et al. (2020) 'Effect of geometries on the heat transfer characteristics of flat-plate micro heat pipes', Applied Thermal Engineering, 180, p. 115796. Available at: https://doi.org/10.1016/j.applthermaleng.2020.115796.

Wang, Q. et al. (2016) 'A critical review of thermal management models and solutions of lithium-ion batteries for the development of pure electric vehicles', Renewable and Sustainable Energy Reviews. Elsevier Ltd, pp. 106–128. Available at: https://doi.org/10.1016/j.rser.2016.05.033.

Wang, X. et al. (2022) 'A Review of the Power Battery Thermal Management System with Different Cooling, Heating and Coupling System', Energies. MDPI. Available at: https://doi.org/10.3390/en15061963.

Wang, Y. et al. (2022) 'Study on the Influence of Flat Heat Pipe Structural Parameters in Battery Thermal Management System', Frontiers in Energy Research, 9. Available at: https://doi.org/10.3389/fenrg.2021.797664.

Weragoda, D.M. et al. (2023) 'A comprehensive review on heat pipe based battery thermal management systems', Applied Thermal Engineering. Elsevier Ltd. Available at: https://doi.org/10.1016/j.applthermaleng.2023.120070.

Wikipedia (2025) Acetone (data page). Available at: https://en.wikipedia.org/wiki/Acetone_(data_page) (Accessed: 13 September 2025).

Wu, J., Zhou, G. and Wang, M. (2020) 'A comprehensive assessment of refrigerants for cabin heating and cooling on electric vehicles', Applied Thermal Engineering, 174. Available at: https://doi.org/10.1016/j.applthermaleng.2020.115258.

Wu, Q., Huang, R. and Yu, X. (2023) 'Measurement of thermophysical parameters and thermal modeling of 21,700 cylindrical battery', Journal of Energy Storage, 65. Available at: https://doi.org/10.1016/j.est.2023.107338.

Xia, G. et al. (2011) 'Optimum thermal design of microchannel heat sink with triangular reentrant cavities', Applied Thermal Engineering, 109, pp. 640-646. Available at: https://doi.org/10.1016/j.applthermaleng.2010.12.022

Xu, Y. et al. (2023) 'Experimental and Simulation Research on Heat Pipe Thermal Management System Coupled with Battery Thermo-Electric Model', Processes, 11(4). Available at: https://doi.org/10.3390/pr11041204.

Zhang, Z. et al. (2018) 'The solutions to electric vehicle air conditioning systems: A review', Renewable and Sustainable Energy Reviews. Elsevier Ltd, pp. 443–463. Available at: https://doi.org/10.1016/j.rser.2018.04.005.